Composite Structures 374 (2025) 119710

Contents lists available at ScienceDirect

Composite Structures

journal homepage: www.elsevier.com/locate/compstruct

Enhanced compressive performance and energy absorption in SLM-fabricated 316L arrowhead auxetics via tendon and stuffer geometry modification

Junsong Wang [a], Cristoforo Demartino [b,*], Antonio P. Sberna [c], Liming Jiang [a], Asif Usmani [a]

[a] Department of Building Environment and Energy Engineering, The Hong Kong Polytechnic University, Kowloon, Hong Kong, China
[b] Department of Architecture, Roma Tre University, Largo G. B. Marzi 10, 00153 Rome, Italy
[c] Department of Structural, Geotechnical and Building Engineering, Politecnico di Torino, Corso Duca degli Abruzzi 24, 10129 Turin, Italy

ARTICLE INFO

Keywords:
Arrowhead structures
Auxetic metamaterials
Selective Laser Melting (SLM)
Finite Element Modeling (FEM)
Compressive behavior
SHPB
Protective applications

ABSTRACT

This study systematically investigates how tailoring the geometry of double-arrowhead auxetic lattice structures — specifically by reducing tendon dimensions while enlarging stuffers — impacts their compressive behavior and energy absorption capabilities. Specimens were fabricated from 316L stainless steel using Selective Laser Melting (SLM) at target relative densities of 5%, 10%, and 15%. We compare the performance of a baseline configuration with equal-sized tendons and stuffers (Lat1 N) against a modified configuration featuring smaller tendons and larger stuffers (Lat1 S). The mechanical response was characterized through a combination of experimental testing, including quasi-static and dynamic (Split Hopkinson Pressure Bar, SHPB) compression, and validated Finite Element Modeling (FEM) analyses, focusing on deformation mechanisms, energy absorption efficiency, Poisson's ratio evolution, and failure modes. Results confirm that increasing relative density significantly enhances the mechanical properties of both auxetic lattice designs. Critically, the geometrically modified Lat1 S configuration consistently demonstrated superior mechanical performance over the baseline Lat1 N, particularly at higher relative densities. For instance, at 15% relative density, Lat1 S exhibited a quasi-static plateau stress of 42 MPa (21% higher than Lat1 N's 35 MPa) and a dynamic plateau stress of 48 MPa under $P = 0.25$ MPa impact (24% higher than Lat1 N's 38.5 MPa). Correspondingly, the yield stresses for Lat1 S were 42.49 MPa (quasi-static) and 48.98 MPa (dynamic at $P = 0.25$ MPa), exceeding the respective Lat1 N values (36.5 MPa and 41.24 MPa). Furthermore, the enhanced design (Lat1 S) achieved superior energy management, reaching an energy absorption per volume (W) of 10.67 MJ/m^3 and a specific energy absorption (SEA) up to 32 J/g, approximately 20% greater than Lat1 N at higher densities. Both configurations exhibited significant strain rate sensitivity, with the dynamic increase factor (DIF) ranging from 1.15 to 1.85 across the tested rates. The improved compressive resistance and energy absorption in Lat1 S are attributed to the enhanced load distribution facilitated by the larger stuffers, highlighting a promising strategy for optimizing auxetic metamaterials for protective applications.

1. Introduction

The continuous demand for lightweight materials offering superior performance in protective applications, such as advanced body armor and impact-resistant vehicle components, necessitates the exploration of innovative material solutions [1]. Within this context, auxetic materials, characterized by their unique negative Poisson's ratio, represent a highly promising class of engineered materials possessing mechanical properties that can surpass those of conventional counterparts [2–7]. These materials exhibit the counterintuitive behavior of expanding laterally when stretched longitudinally or contracting laterally when compressed—a stark contrast to the positive Poisson's ratio observed in most engineering materials [8]. This unique characteristic renders auxetic structures exceptionally well-suited for applications demanding robust impact resistance and efficient energy dissipation, including protective gear and specialized structural panels [8,9].

Additive Manufacturing (AM), particularly powder bed fusion techniques like Selective Laser Melting (SLM), is pivotal in realizing the potential of auxetic metamaterials by enabling the fabrication of their

* Corresponding author.
E-mail addresses: jun-song.wang@connect.polyu.hk (J. Wang), cristoforo.demartino@me.com (C. Demartino), antonio.sberna@polito.it (A.P. Sberna), liming.jiang@polyu.edu.hk (L. Jiang), asif.usmani@ed.ac.uk (A. Usmani).

https://doi.org/10.1016/j.compstruct.2025.119710
Received 10 April 2025; Received in revised form 12 June 2025; Accepted 27 September 2025
Available online 16 October 2025

often complex architectures with high fidelity and material efficiency [10,11]. Producing such intricate geometries presents significant obstacles for traditional manufacturing methods, which frequently face limitations related to achievable precision, scalability, and material versatility [8]. SLM technology, however, has revolutionized the fabrication landscape, allowing the direct production of complex lattice structures with precisely controlled features from digital models [12–16]. As a subset of Powder Bed Fusion (PBF) processes, SLM facilitates the layer-by-layer construction of metallic components, offering exceptional control over geometric accuracy and material distribution [1,17]. This manufacturing capability is indispensable for auxetic metamaterials, where subtle variations in geometric details can critically influence the overall mechanical performance [8,17].

Auxetic metamaterials fabricated via SLM are predominantly designed using strut-based configurations. These configurations typically involve intricate lattice architectures, such as re-entrant honeycombs, chiral patterns, and arrowhead structures, which achieve a negative Poisson's ratio through specific microstructural deformation mechanisms like hinge rotation or strut bending [18–28]. Consequently, strut-based designs are widely employed to harness auxetic properties, offering distinct advantages in mechanical performance and energy absorption capacity [29–34]. Such auxetics often excel under large deformations and can provide enhanced stiffness and fracture resistance, making them highly effective for applications requiring superior energy dissipation and impact mitigation [8,9]. Among these designs, arrowhead structures have garnered significant research interest due to their characteristic deformation mechanisms and notable energy absorption potential. Arrowhead configurations, including double arrowhead and star-shaped variants, utilize a re-entrant geometry that facilitates a pronounced negative Poisson's ratio through the coordinated rotation and bending of constituent struts under axial loading [35–37]. Current research endeavors often focus on optimizing the geometric parameters of arrowhead structures to further enhance mechanical performance — for example, increasing stiffness while preserving auxetic behavior — and to improve energy dissipation during dynamic impact events [9,38]. Furthermore, hybrid designs integrating arrowhead elements with other lattice topologies (e.g., chiral or missing rib structures) are being actively explored to achieve tailored mechanical responses and multifunctional capabilities [39,40].

Understanding the mechanical behavior of SLM-fabricated lattice structures under both quasi-static and dynamic loading conditions is crucial, particularly concerning their energy absorption capabilities [1,8]. Under quasi-static loading, these structures typically exhibit significant yield and plateau stresses that scale predictably with relative density, indicating their suitability for energy absorption applications requiring controlled deformation. Dynamic loading scenarios, often evaluated using techniques like the Split-Hopkinson Pressure Bar (SHPB), frequently reveal pronounced strain-rate sensitivity and enhanced energy dissipation characteristics under high-velocity impacts, properties essential for effective performance in protective systems [8,17,41]. Consequently, a comprehensive understanding of compressive behavior across a range of loading rates is vital for optimizing auxetic metamaterials for protective applications, where components may be subjected to diverse impact forces and velocities [42–46]. These findings underscore the necessity of characterizing both quasi-static and dynamic responses to effectively design auxetic metamaterials for real-world engineering challenges. While macroscopic stress, strain, and strain rate are commonly used for characterizing the overall mechanical response of cellular materials, it is important to acknowledge that for highly heterogeneous lattice structures, particularly at lower relative densities, the local stress and strain fields can be complex and non-uniform. Our analysis focuses on average nominal values, which represent the overall structural behavior, with comprehensive FEM simulations providing insights into the localized deformation mechanisms.

Beyond the macroscopic geometric design, the inherent microstructure of SLM-fabricated components plays a critical role in dictating their resultant mechanical properties. The rapid melting and solidification cycles characteristic of the SLM process can induce unique microstructural features, including fine grain structures, significant residual stresses, and potential porosity, all of which substantially influence the material's performance under both quasi-static and dynamic loads [47–50]. To refine these microstructures and optimize performance, post-processing steps such as heat treatment are commonly employed. These treatments can effectively alleviate detrimental residual stresses, enhance microstructural homogeneity, and improve material ductility, thereby leading to more predictable and robust mechanical behavior in the final lattice structures [51,52].

In addition to microstructural considerations, the overall quality of SLM-fabricated lattice structures is heavily dependent on manufacturing attributes like dimensional accuracy and surface roughness. Achieving high dimensional accuracy ensures that the as-built geometry faithfully replicates the intended design specifications, a prerequisite for attaining the targeted mechanical performance and auxetic behavior [53,54]. Conversely, surface roughness, an inherent outcome of the layer-wise fabrication process, can act as initiation sites for cracks, potentially compromising the structural integrity and adversely affecting the energy absorption capacity of the lattice structures [1,8]. Careful control over these factors is therefore essential for reliable performance.

Despite considerable progress, a critical knowledge gap persists regarding how specific, targeted geometric variations within double-arrowhead auxetic structures — particularly adjustments to tendon thickness and stuffer size — influence their comprehensive compressive response under both quasi-static and dynamic loading conditions. While previous research has demonstrated the general tunability of mechanical behavior in various auxetic geometries through parameter adjustments, studies focusing specifically on the interplay between tendon thickness and stuffer size within double-arrowhead configurations, across different loading rates, are scarce [55]. Furthermore, the combined influence of these distinct geometric parameters and the overall relative density on the performance of SLM-fabricated double-arrowhead structures remains largely unexplored territory.

This study aims to directly address this knowledge gap by systematically investigating the quasi-static and dynamic compressive behavior of SLM-fabricated 316L stainless steel double-arrowhead lattice structures featuring specific geometric modifications: namely, reduced tendon dimensions coupled with enlarged stuffers. We examine these structures at relative densities of 5%, 10%, and 15% to understand how density interacts with these structural modifications, thereby influencing deformation mechanisms, energy absorption efficiency, and Poisson's ratio behavior, as detailed in Section 2. Utilizing both experimental compression tests (quasi-static and SHPB) and validated Finite Element Modeling (FEM), we seek to elucidate the precise effects of these geometric changes on mechanical performance. By systematically altering the tendon and stuffer dimensions (Section 2.1), this research endeavors to identify optimized designs for enhanced energy absorption and impact resistance. The integration of experimental data with simulation results (Sections 3 and 4) provides a comprehensive understanding of the structure–property relationships, paving the way for informed design guidelines for these high-performance metamaterials. Furthermore, the effects of relative density and strain rate sensitivity on mechanical performance are discussed in Section 5. Ultimately, this work contributes to the broader effort of leveraging additive manufacturing to create advanced auxetic structures tailored for demanding protective applications, thereby advancing the frontiers of materials science and engineering design (Section 6).

2. Experimental procedure

This section details the design, fabrication, and testing methodologies employed to investigate the double-arrowhead auxetic lattice structures.

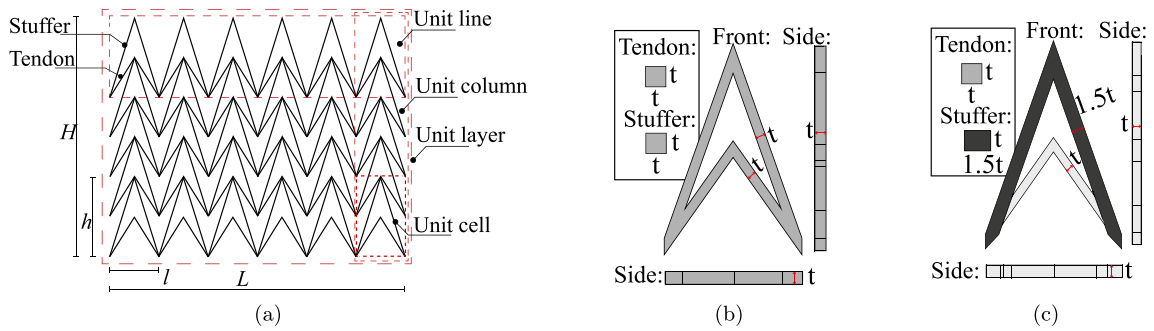

Fig. 1. Design of the double-arrowhead auxetic structure. (a) 2D schematic illustrating key components (tendons, stuffers) and unit cell parameters (L, H, l, h). (b) Unit cell for the baseline Lat1 N configuration (equal tendon and stuffer sizes). (c) Unit cell for the modified Lat1 S configuration (larger stuffer, smaller tendon).

2.1. Auxetic lattice arrowhead structure design

The fundamental geometry of the double-arrowhead auxetic lattice structure investigated in this study is illustrated in Fig. 1(a). This 2D representation highlights the key components, namely the tendons and stuffers, which constitute the unit cell. The figure also defines essential geometric parameters: structure length (L), height (H), unit cell length (l), and unit cell height (h). These parameters, along with the number of cells in height ($N_r = 5$) and length ($N_c = 6$), define the overall lattice dimensions ($H = 28$ mm length, $L = 22.4$ mm height) and are intrinsically linked to the density control algorithm used for design. Two distinct configurations were developed for comparison: a baseline configuration (Lat1 N) with equally sized tendons and stuffers (Fig. 1(b)), and a modified configuration (Lat1 S) featuring smaller tendons and larger stuffers (Fig. 1(c)).

The strut dimensions are defined relative to a base thickness t. Critically, the value of t is not fixed but is iteratively adjusted by our density control algorithm (Algorithm 1) for each specific configuration (Lat1N or Lat1S) and target relative density. Thus, while Lat1 N has $h_s \times w_s = h_t \times w_t = t \times t$ and Lat1S has stuffer dimensions $1.5t \times t$ and tendon dimensions $t \times t$, the precise value of t will differ between configurations and target densities to achieve the desired overall relative density. For the 3D structure, the unit cell is arrayed in three dimensions, involving $N_L = 26$ layers (13 along the length and 13 along the width) to form a cubic lattice. These specific dimensions were chosen to effectively capture the auxetic behavior while adhering to the constraints of the experimental testing equipment, as detailed later.

2.1.1. Design for target relative density

Achieving precise control over the relative density (ρ_R) is crucial for tailoring the mechanical properties of lattice structures. To this end, an iterative algorithm (Algorithm 1) was developed and implemented to systematically adjust the tendon and stuffer dimensions. This algorithm minimizes deviations from the target ρ_R while maintaining the intended geometric ratios defining the Lat1 N and Lat1 S configurations. The algorithm functions by iteratively calculating an estimated current density (ρ_C) based on nominal strut volumes and applying a correction factor ($G(i)$) to account for material volume in overlapping regions between struts. The $G(i)$ function aids convergence by allowing controlled adjustments to these overlap volumes. For accurate geometric modeling and volume calculation, Rhinoceros 3D software (Robert McNeel & Associates) was integrated into the workflow. Within Rhino, Boolean operations were employed to precisely remove overlapping volumes, yielding the actual material volume (V_{material}) of the non-overlapping structure. This volume was then used to calculate the intermediate relative density ($\rho_M = V_{\text{material}}/V_{\text{structure}}$), where $V_{\text{structure}} = L \times W \times H$. The algorithm iteratively refines the strut dimensions (h_s, w_s, h_t, w_t) based on the comparison between ρ_M and the target ρ_R, continuing until the difference falls below a predefined tolerance (0.0001), thus ensuring high fidelity between the designed and target relative densities.

Algorithm 1 Density control algorithm for double-arrowhead lattice structure design.

procedure DENSITY CONTROL(TargetDensity ρ_R)
  Input: Target relative density ρ_R, Initial geometric parameters (cell dimensions, strut ratios).
  Output: Finalized strut dimensions (h_s, w_s, h_t, w_t) achieving ρ_R.
  Initialize target relative density ρ_R.
  Initialize structural parameters: N_L (layers), N_r (rows), N_c (columns), l (cell length), h (cell height), L, H, W (overall dimensions).
  for each iteration $i = 1, 2, \ldots$ **do**
    Estimate current density ρ_C using nominal volumes and overlap correction $G(i)$:

$$\rho_C = \frac{N_L \times N_r \times N_c \times F(l,h) - G(i)}{W \times H \times L}$$

    where $F(l,h) = h_s w_s L_s + h_t w_t L_t$ (nominal strut volumes), with $L_t = \sqrt{l^2 + 4h^2}$, $L_s = \sqrt{l^2 + h^2}$.
    Determine current trial strut dimensions based on target ρ_R and configuration type (N or S).
    Model the structure in Rhino 3D using current dimensions (h_t, w_t, L_t) and (h_s, w_s, L_s) within the bounding box (L, H, W).
    Perform Boolean operations in Rhino to remove overlaps and calculate precise material volume V_{material}.
    Compute intermediate relative density $\rho_M = V_{\text{material}}/(L \times H \times W)$.
    Compare calculated density ρ_M with target ρ_R.
    if $|\rho_C - \rho_M| > 0.0001$ **then** ▷ Refine overlap estimation
      Adjust overlap function $G(i) = G(i) + \Delta G$, where ΔG depends on the difference $\rho_C - \rho_M$.
      Continue ▷ Next iteration with refined $G(i)$
    else if $|\rho_R - \rho_M| > 0.0001$ **then** ▷ Adjust strut dimensions
      Adjust strut dimensions $\{h_s, w_s, h_t, w_t\}$ based on the deviation $\rho_R - \rho_M$, maintaining N/S ratio.
      Recalculate $G(i)$ based on new dimensions.
      Continue ▷ Next iteration with adjusted dimensions
    else ▷ Target density achieved
      Finalize structure with density $\rho_M \approx \rho_R$.
      Return finalized strut dimensions $\{h_s, w_s, h_t, w_t\}$.
      Exit For
    end if
  end for
end procedure

2.2. Specimen manufacturing and fabrication

The auxetic lattice structures investigated, designated Lat1, were designed using the methodology described in Section 2.1 and Algorithm 1. Specimens were targeted for three relative densities: 5%, 10%, and 15%. For each density, both the standard (N: equal tendon/stuffer size) and modified (S: larger stuffer, smaller tendon) configurations were fabricated. Specimen nomenclature follows the format Lat1, X, $\rho_R = Y\%$, where X is N or S, and Y is the target relative density. Table 1 visually summarizes the unit cell designs and the resulting 3D structure architecture.

The 3D lattice (Table 1) was generated by replicating a derived 3D unit cell (formed by duplicating, rotating, and inverting the 2D cell) along three orthogonal axes. The final structure comprised 5 cells in height ($H_n = 5$) and 6 cells in both length ($L_n = 6$) and width ($W_n = 6$),

Table 1
Specimen design concepts: unit cells and resulting lattice structure.

Configuration		Unit cell		Structure
Strut type		Front view	Perspective view	Perspective view
Baseline (Equal Tendon/Stuffer)	N			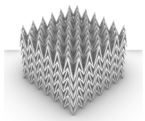
Modified (Larger Stuffer/Smaller Tendon)	S			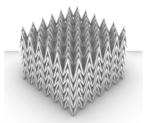
Structure Size ($L \times W \times H$)		28 mm × 28 mm × 22.4 mm		
Cell Count ($L_n \times W_n \times H_n$)		6 × 6 × 5		
Target Relative Density (ρ_R)		5%, 10%, 15%		

Table 2
Additively manufactured 316L stainless steel specimens used for testing. The structure size is 28 mm × 28 mm × 22.4 mm.

Name	Lat1, N, $\rho_R = 5\%$	Lat1, S, $\rho_R = 5\%$	Lat1, N, $\rho_R = 10\%$	Lat1, S, $\rho_R = 10\%$	Lat1, N, $\rho_R = 15\%$	Lat1, S, $\rho_R = 15\%$
Front View				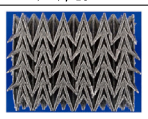		
Top View	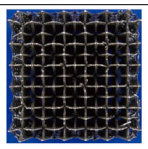	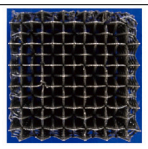	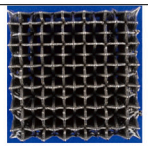	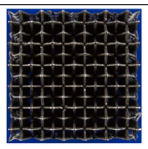	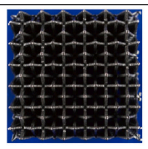	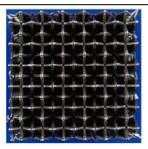
Perspective	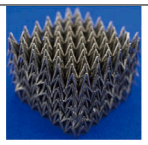	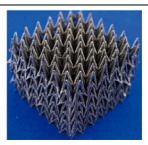	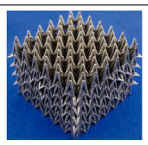	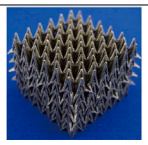	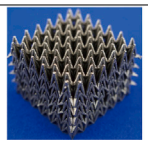	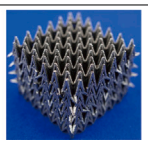

resulting in overall dimensions of 22.4 mm (height) × 28 mm (length) × 28 mm (width). Table 2 shows the resulting additively manufactured specimens prepared for testing. For each combination of configuration (N/S) and relative density (5/10/15%), four identical specimens were produced. Three specimens from each set were subsequently tested: one under quasi-static compression and two under dynamic compression (SHPB) at different impact pressures.

All specimens were fabricated from 316L stainless steel powder using Selective Laser Melting (SLM) on a BLT-A300 machine (Xian Bright Laser Technologies Ltd., P.R. China), shown in Fig. 2. The gas-atomized 316L powder possessed a particle size distribution of 20–50 μm. Uniform processing parameters were applied for all builds based on sliced STL models derived from the Rhino designs. The SLM process involved layer-by-layer selective melting at a laser scanning speed of 960 mm/s, employing a laser power ranging from 150–290 W and a layer thickness of 80 μm. To mitigate oxidation during fabrication, the build chamber was maintained under an inert argon atmosphere.

Following SLM fabrication and removal from the build plate, the specimens underwent a post-processing heat treatment (tempering) to relieve residual stresses induced during the rapid heating and cooling cycles of the AM process. The tempering protocol involved heating the specimens at a rate of 10 °C/min to 700 °C, holding for 30 min, further heating to 1050 °C and holding for 4 h,. followed by controlled furnace cooling, adapted from standard practices for additively manufactured 316L stainless steel [56,57].

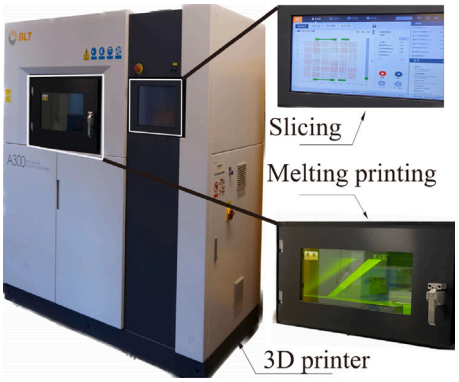

Fig. 2. BLT-A300 Selective Laser Melting (SLM) machine used for specimen fabrication.

2.3. Quasi-static compressive tests

Quasi-static uniaxial compression tests were performed using a universal testing machine equipped with a 100 kN load cell (Fig. 3). Testing was conducted at a constant crosshead displacement rate of 0.5 mm/min, corresponding to an initial nominal strain rate of $\dot{\varepsilon} \approx 4\times10^{-4}\ s^{-1}$ (calculated based on the initial specimen height). Specimens were carefully centered between hardened steel platens to ensure uniform load application and minimize misalignment. To reduce friction

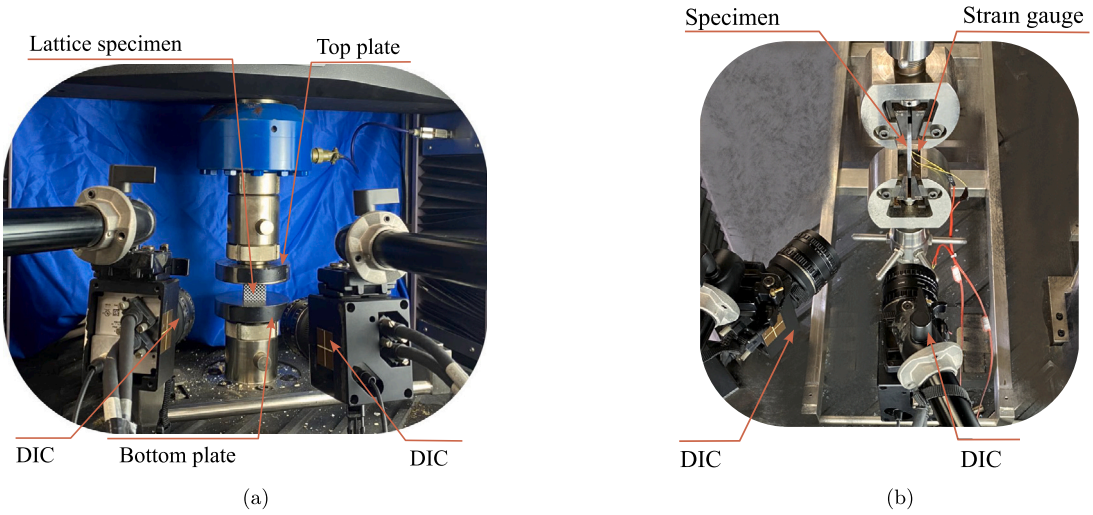

Fig. 3. Experimental setup for quasi-static tests. (a) Universal testing machine configuration for compression. (b) Digital Image Correlation (DIC) setup for full-field strain measurement.

between the specimen surfaces and the platens, petroleum jelly was applied as a lubricant. Each test continued until either the load limit of the machine (98 kN) was approached or significant densification occurred, typically considered around a nominal strain of $\varepsilon_N = 65\%$. Nominal strain was calculated as $\varepsilon_N = \Delta H / H_0$, where ΔH is the axial displacement and H_0 is the initial specimen height. Nominal stress was calculated as $\sigma_N = F/A_0$, where F is the measured reaction force and $A_0 = L \times W$ is the initial cross-sectional area of the bounding box.

Full-field surface deformation was monitored throughout the tests using a Digital Image Correlation (DIC) system. This system employed two high-resolution digital cameras (2448 × 2048 pixels) synchronized to capture images of a speckle pattern applied to the specimen surface, enabling subsequent calculation of displacement and strain fields (Fig. 3(b)).

2.4. Split-Hopkinson pressure bar (SHPB) dynamic tests

Dynamic compressive behavior was characterized using a Split-Hopkinson Pressure Bar (SHPB) apparatus to assess impact resistance and energy absorption at high strain rates.

2.4.1. Dynamic test setup

The SHPB setup, depicted schematically and photographically in Fig. 4, consisted of a striker bar, an incident bar, and a transmission bar, all made of high-strength aluminum alloy. The bars had respective lengths of 0.8 m, 3.0 m, and 2.0 m, and a uniform diameter of 40 mm. Specimens were sandwiched between the incident and transmission bars. Dynamic tests were conducted at two distinct impact conditions, generated by striker launch pressures of $P = 0.15$ MPa and $P = 0.25$ MPa, to investigate the influence of strain rate. This configuration allows for precise measurement of forces and displacements experienced by the specimen during high-velocity impact events [58]. A high-speed camera synchronized with the impact event was used to capture the deformation process (Fig. 4(b)).

2.4.2. Stress wave analysis

The fundamental principle of SHPB testing relies on one-dimensional elastic wave propagation theory. When the striker impacts the free end of the incident bar, it generates a compressive stress wave (ε_i) that travels towards the specimen. Upon reaching the specimen interface, part of the wave is reflected back into the incident bar as a tensile wave (ε_r), while the remaining portion is transmitted through the specimen into the transmission bar as a compressive wave (ε_t). Strain gauges mounted on the incident and transmission bars measure these time-resolved strain pulses.

Assuming one-dimensional wave propagation and neglecting wave dispersion effects initially, the nominal stress at the front (incident bar/specimen) interface ($\sigma_{N,2D}$) and the rear (specimen/transmission bar) interface ($\sigma_{N,1D}$) can be calculated using the recorded strains [59]:

$$\sigma_{N,1D}(t) = \frac{EA_b}{A_s}\varepsilon_t(t) \quad \text{(1D/Rear Interface Stress)} \tag{1a}$$

$$\sigma_{N,2D}(t) = \frac{EA_b}{A_s}(\varepsilon_i(t) + \varepsilon_r(t)) \quad \text{(2D/Front Interface Stress)} \tag{1b}$$

where E is the Young's modulus of the bar material, A_b is the cross-sectional area of the bars, and A_s is the initial cross-sectional area of the specimen. Under the condition of dynamic stress equilibrium within the specimen ($\sigma_{N,1D}(t) \approx \sigma_{N,2D}(t)$), the average nominal stress across the specimen ($\sigma_{N,3D}$) can be calculated as:

$$\sigma_{N,3D}(t) = \frac{\sigma_{N,1D}(t) + \sigma_{N,2D}(t)}{2} = \frac{EA_b}{2A_s}(\varepsilon_i(t) + \varepsilon_r(t) + \varepsilon_t(t)) \quad \text{(3D/Average Stress)} \tag{1c}$$

Stress equilibrium implies the relationship $\varepsilon_t(t) \approx \varepsilon_i(t) + \varepsilon_r(t)$.

The nominal strain ($\varepsilon(t)$) and nominal strain rate ($\dot{\varepsilon}(t)$) experienced by the specimen are determined primarily from the reflected wave:

$$\dot{\varepsilon}(t) = \frac{-2c_b}{L_s}\varepsilon_r(t) \tag{1d}$$

$$\varepsilon(t) = \int_0^t \dot{\varepsilon}(\tau)d\tau = \frac{-2c_b}{L_s}\int_0^t \varepsilon_r(\tau)d\tau \tag{1e}$$

where L_s is the initial length (height) of the specimen, and $c_b = \sqrt{E/\rho_b}$ is the elastic longitudinal wave speed in the bar material (ρ_b is the density of the bar material).

The Average Strain Rate (ASR) over a specific time interval (typically after initial wave reverberations establish equilibrium) is often used to characterize the overall loading rate [59]:

$$ASR = \frac{1}{t-\tau}\int_\tau^t \dot{\varepsilon}(\xi)d\xi = \frac{-2c_b}{L_s(t-\tau)}\int_\tau^t \varepsilon_r(\xi)d\xi \tag{2}$$

where the integration interval $[\tau, t]$ is chosen within the period where the strain rate is relatively constant (here, τ was typically set around 75 μs).

Accurate alignment of the measured pulses requires accounting for the wave transit time through the specimen (ΔT). The arrival time of

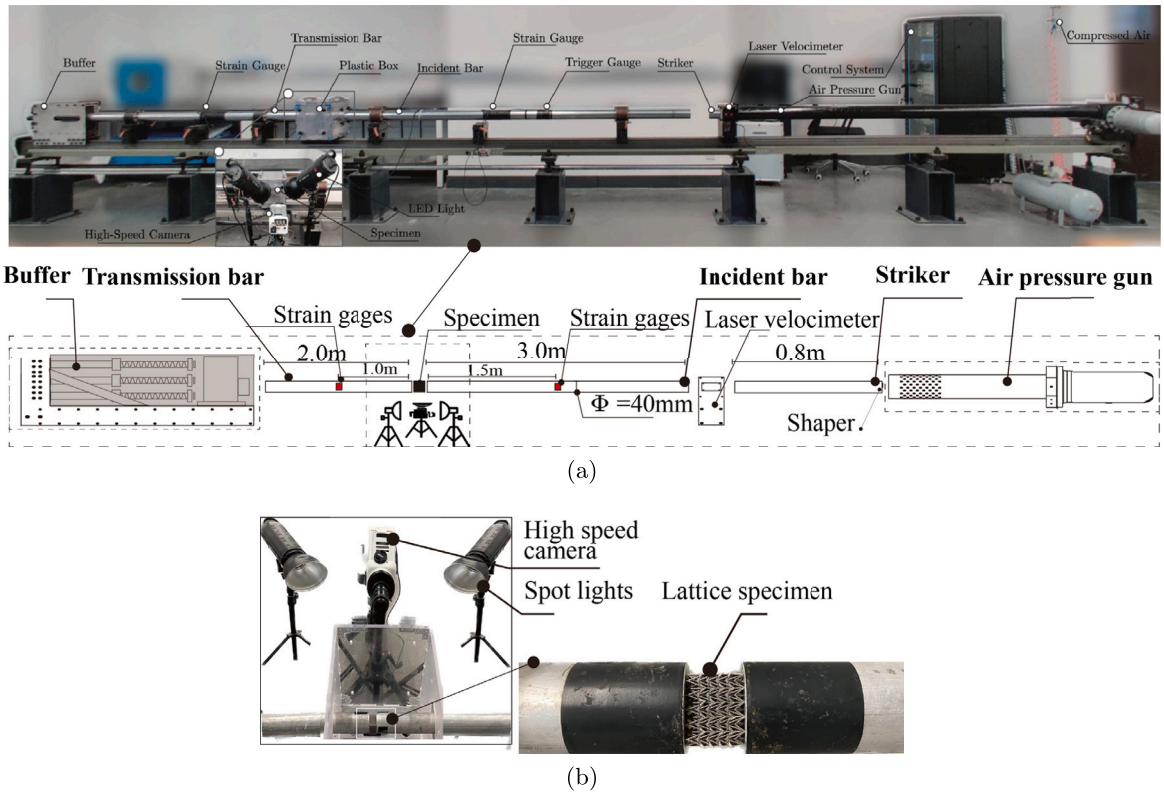

Fig. 4. Split-Hopkinson Pressure Bar (SHPB) apparatus. (a) Schematic diagram and photograph of the setup, illustrating the striker, incident bar, specimen, and transmission bar. (b) Close-up view showing the specimen positioned between the bars and the high-speed camera for recording deformation.

the incident pulse (T_i) at the front face relates to the arrival time of the transmitted pulse (T_t) at the rear face by:

$$T_i = T_t - \Delta T \tag{3}$$

where ΔT is estimated as:

$$\Delta T = \frac{H_0}{c_{\text{specimen}}} \approx \frac{H_0}{\sqrt{E_N/\rho_{\text{eff}}}} \tag{4}$$

Here, H_0 is the initial specimen height, c_{specimen} is the effective wave speed in the lattice, E_N is the quasi-static elastic modulus of the lattice, and $\rho_{\text{eff}} = \rho_{PR}\rho_{\text{solid}}$ is the effective density of the lattice structure (with ρ_{PR} being the measured relative density of the printed specimen and ρ_{solid} the density of solid 316L).

2.4.3. Stress equilibrium verification

Ensuring dynamic stress equilibrium across the specimen length is crucial for the validity of SHPB results derived using the simplified 1D wave theory. Significant deviations from equilibrium indicate that the stress state is non-uniform, potentially invalidating the calculated stress–strain response. Equilibrium is quantitatively assessed using the relative stress difference parameter $\zeta(t)$ [59]:

$$\zeta(t) = \frac{|\sigma_{N,2D}(t) - \sigma_{N,1D}(t)|}{\sigma_{N,avg}(t)} \times 100\% \approx \frac{2|\varepsilon_i(t) + \varepsilon_r(t) - \varepsilon_t(t)|}{|\varepsilon_i(t) + \varepsilon_r(t) + \varepsilon_t(t)|} \times 100\% \tag{5}$$

where $\sigma_{N,avg}(t)$ is typically taken as $\sigma_{N,3D}(t)$. Stress equilibrium is considered adequately achieved when $\zeta(t)$ remains below a threshold, commonly accepted as 5%, during the primary deformation phase. For the tests reported herein, $\zeta(t)$ was monitored and generally remained below 5% after the initial loading ramp, confirming the validity of the derived dynamic stress–strain curves for both Lat1 N and Lat1 S configurations.

2.4.4. SHPB data calibration and dispersion correction

To ensure accuracy, the SHPB data acquisition system requires careful calibration. Potential sources of error include strain gauge misalignment, bonding imperfections, and electronic noise [60,61]. A key calibration step involves comparing the measured amplitude of the incident strain pulse (ε_i) with the theoretical amplitude (ε_p) expected based on the measured striker velocity (v_i). The theoretical amplitude is given by:

$$\varepsilon_p = \frac{v_i}{2c_b} \tag{6}$$

where v_i was measured using a laser velocimeter immediately before impact. Calibration tests were performed without a specimen, using the same impact pressures ($P = 0.15$ MPa and $P = 0.25$ MPa) as the main experiments. Fig. 5(a) shows typical incident pulses recorded during calibration, with the stable plateau region (e.g., 150–230 μs) used to determine the average measured ε_i. Fig. 5(b) confirms a strong linear correlation between the measured ε_i (averaged over the plateau) and the predicted ε_p, validating the velocity measurement and initial pulse generation. A strain correction factor, K_ε, was calculated as:

$$K_\varepsilon = \frac{\varepsilon_p}{\text{mean}(\varepsilon_i)} \tag{7}$$

The factor K_ε was found to be consistently close to 1, indicating minimal systematic error in the strain measurement [62]. Measured strain signals were subsequently multiplied by K_ε if necessary, although corrections were minor.

Another challenge in SHPB testing is geometric dispersion, where different frequency components of the stress wave travel at slightly different velocities in the bars, distorting the pulse shape, particularly for sharp-fronted waves [63,64]. To mitigate dispersion and achieve a smoother, more controlled loading rate, pulse shaping techniques are employed [65–68]. In this study, a small disk of 1 mm thick hard paper was placed on the impact face of the incident bar. The plastic

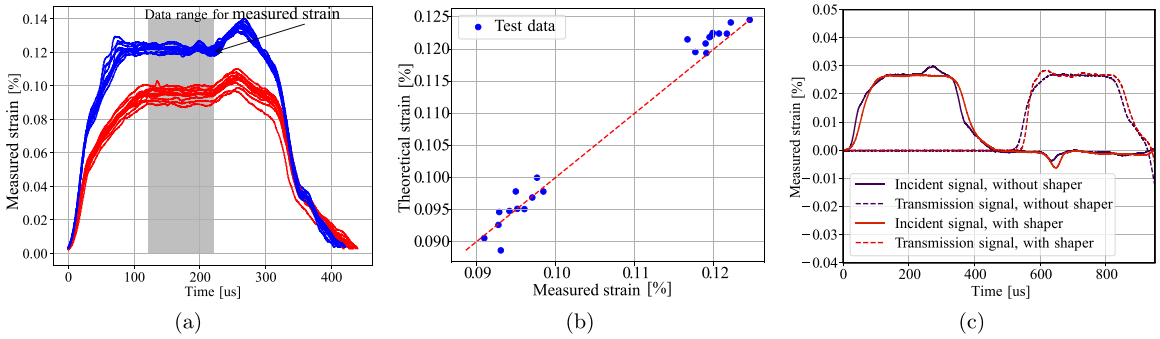

Fig. 5. SHPB calibration and pulse shaping. (a) Incident strain pulses from calibration tests, highlighting the plateau region (150–230 μs) used for analysis. (b) Correlation between predicted (ε_p) and measured (ε_i) incident strain amplitudes. (c) Comparison of incident pulse shapes with and without a 1 mm paper pulse shaper, demonstrating oscillation reduction.

deformation of this 'pulse shaper' upon striker impact modified the input waveform, increasing its rise time and reducing high-frequency oscillations. Fig. 5(c) illustrates the effectiveness of the pulse shaper in generating a smoother, near-trapezoidal incident pulse compared to an unshaped impact, facilitating stress equilibrium and clearer data interpretation.

2.5. Compressive behavior analysis

The mechanical response under compression was analyzed by extracting key parameters from the nominal stress–strain curves.

2.5.1. Compression properties

The compressive behavior of cellular lattice structures, including the auxetic designs studied here, typically exhibits three distinct regimes, as schematically shown in Fig. 6: (1) an initial linear elastic region, (2) a prolonged plastic plateau region where deformation occurs at nearly constant stress, and (3) a final densification region where the stress rises sharply as cell walls crush together [1,8].

The effective elastic modulus (E_N) was determined as the slope of the initial linear portion of the nominal stress–strain curve. The yield point, marking the transition from elastic to plastic behavior, was identified by the nominal stress ($\sigma_{N,Y}$) corresponding to the nominal strain ($\varepsilon_{N,Y}$) at which the curve deviates significantly from linearity. This was practically determined as the stress at the first significant peak or using the 0.2% offset method, whichever yielded a clearer transition. The plateau stress ($\sigma_{N,p}$), representing the average stress sustained during the plastic collapse phase, was calculated by integrating the stress over a defined strain range within the plateau region:

$$\sigma_{N,p} = \frac{1}{\varepsilon_{N,E} - \varepsilon_{N,S}} \int_{\varepsilon_{N,S}}^{\varepsilon_{N,E}} \sigma_N(\varepsilon) d\varepsilon \tag{8}$$

where $[\varepsilon_{N,S}, \varepsilon_{N,E}]$ defines the strain interval for averaging, typically starting near the yield strain ($\varepsilon_{N,S} \geq \varepsilon_{N,Y}$) and ending before the onset of densification. The densification strain ($\varepsilon_{N,D}$) marks the end of the efficient energy absorption phase and the beginning of rapid stress increase. It was identified as the strain at which the energy absorption efficiency (defined below) reaches its maximum value [69].

2.5.2. Energy absorption properties

The energy absorption performance of the lattice structures is a primary focus, particularly for protective applications. Key metrics include the energy absorbed per unit volume (W), the energy absorption efficiency (η), and the specific energy absorption (SEA).

The energy absorbed per unit volume up to a specific nominal strain $\varepsilon_{N,W}$ is calculated by integrating the area under the nominal stress–strain curve [70,71]:

$$W(\varepsilon_{N,W}) = \int_0^{\varepsilon_{N,W}} \sigma_N(\varepsilon) d\varepsilon \tag{9}$$

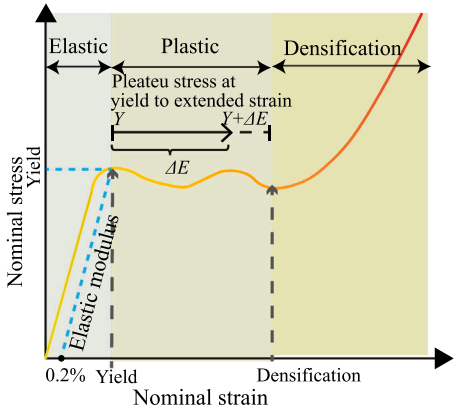

Fig. 6. Schematic nominal stress–strain curve for a typical lattice structure under compression, illustrating the elastic, plateau, and densification stages, along with key parameters: yield point ($\varepsilon_{N,Y}$, $\sigma_{N,Y}$), plateau stress ($\sigma_{N,p}$), and densification strain ($\varepsilon_{N,D}$).

The energy absorption efficiency at strain $\varepsilon_{N,W}$ quantifies how effectively the structure absorbs energy compared to an ideal plastic absorber with the same peak stress ($\sigma_{N,W} = \sigma_N(\varepsilon_{N,W})$) [71–73]:

$$\eta(\varepsilon_{N,W}) = \frac{W(\varepsilon_{N,W})}{\sigma_{N,W}} \tag{10}$$

The densification strain $\varepsilon_{N,D}$ corresponds to the strain at which $\eta(\varepsilon)$ reaches its maximum.

The Specific Energy Absorption (SEA) normalizes the absorbed energy by the mass of the structure, providing a measure of energy absorption capacity on a weight basis. It is calculated using the measured printed relative density ρ_{PR} and the density of the solid base material ρ_{solid} [71,72]:

$$SEA(\varepsilon_{N,W}) = \frac{W(\varepsilon_{N,W})}{\rho_{\text{eff}}} = \frac{W(\varepsilon_{N,W})}{\rho_{PR}\rho_{\text{solid}}} \tag{11}$$

2.5.3. Poisson's ratio analysis

The characteristic auxetic behavior (negative Poisson's ratio) was quantified using data obtained from the DIC system during quasi-static tests. Strain evolution was tracked at multiple discrete points located on the external surface of a central unit cell, as illustrated in Fig. 7. Five points (i = 1 to 5) were tracked along a horizontal line to measure average lateral strain ($\varepsilon_{lateral}$), and six points (j = 1 to 6) were tracked along a vertical line to measure average axial strain (ε_{axial}). The nominal Poisson's ratio (ν_N) was then calculated as the negative ratio

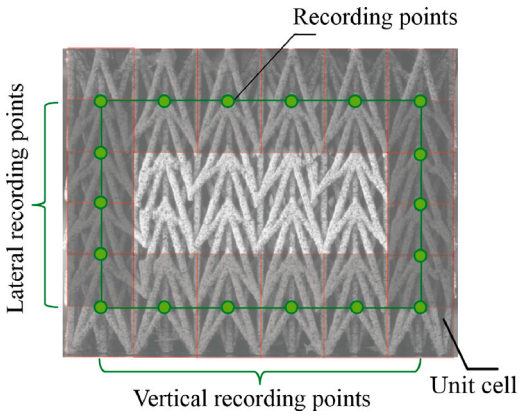

Fig. 7. Location of virtual points tracked via Digital Image Correlation (DIC) on the surface of a central unit cell for calculating Poisson's ratio. Red points (i = 1–5) track lateral deformation, while blue points (j = 1–6) track axial deformation.

of the average lateral strain to the average axial strain:

$$\nu_N = -\frac{\varepsilon_{lateral}}{\varepsilon_{axial}} = -\frac{(\sum_{i=1}^{5} \varepsilon_{N,i})/5}{(\sum_{j=1}^{6} \varepsilon_{N,j})/6} \tag{12}$$

where $\varepsilon_{N,i}$ are the nominal strains at the lateral points and $\varepsilon_{N,j}$ are the nominal strains at the vertical points, derived from the DIC displacement fields relative to the initial specimen dimensions.

2.6. Base material characterization

To obtain accurate material properties for the constitutive modeling used in the Finite Element (FE) simulations (Section 4), quasi-static tensile and compressive tests were performed on specimens made from the same 316L stainless steel powder and fabricated using the same SLM process and post-processing heat treatment as the lattice structures. Standard dog-bone shaped specimens (Fig. 8(a)) were used for tensile tests according to relevant standards, while solid prism-shaped specimens (Fig. 8(b)) were used for compression tests. Two tests were conducted for each loading condition using the same universal testing machine and DIC setup described in Section 2.3. Tensile tests provided data for determining Young's modulus, yield strength, and strain hardening behavior, while compression tests characterized the material response under compressive stress states relevant to lattice deformation. The DIC system was crucial for accurately measuring strain, particularly in the post-yield regime. The resulting stress–strain data formed the basis for calibrating the Johnson–Cook material model used in the FE analyses.

3. Experimental results

This section presents the experimental findings, beginning with an assessment of the fabricated specimen quality and proceeding to the detailed analysis of their compressive mechanical behavior under both quasi-static and dynamic loading conditions.

3.1. Comparison of designed versus as-printed relative density

Achieving perfect fidelity between the digital design and the physical part in Additive Manufacturing, particularly SLM, remains challenging. Several inherent process characteristics contribute to geometric deviations in the as-printed lattice structures. These include material shrinkage during rapid solidification, the adherence of partially melted or unmelted powder particles to strut surfaces, and surface irregularities such as strut waviness and overall roughness [1,17]. Such imperfections can significantly influence the final mechanical properties, notably strength and stiffness. Micro-computed tomography studies have previously documented these deviations, revealing localized regions of excess or insufficient material compared to the original CAD model [74].

Furthermore, the layer-wise nature of SLM introduces the "staircase effect", particularly noticeable on inclined or curved surfaces (illustrated schematically in Fig. 9). This effect arises from the discrete approximation of smooth geometries by stacked layers, leading to stepped surfaces. Unmelted powder particles tend to adhere more readily to these stepped features, especially on downward-facing surfaces, further contributing to dimensional inaccuracies and increased surface roughness [75,76]. Scanning Electron Microscopy (SEM) images of the fabricated Lat1 struts (Fig. 10) clearly show this rough surface morphology resulting from attached powder particles. Feature size measurements from SEM images (resolution ±1 μm) confirmed variations in strut dimensions compared to the design intent.

To quantify the overall geometric deviation, the actual relative density (ρ_{PR}) of each fabricated specimen was determined by measuring its mass and dividing by the theoretical mass of a solid block with the same bounding box dimensions ($L \times W \times H$). Fig. 11(a) compares the target relative densities (ρ_R) with the measured as-printed relative densities (ρ_{PR}) for both Lat1 N and Lat1 S configurations. Consistently, the printed specimens exhibited higher relative densities than designed, with an average discrepancy of approximately 6%. This observation aligns well with previous findings; for instance, Al-Ketan et al. [75] reported a similar discrepancy of about 7% for SLM-fabricated lattices with a target relative density of 10%. This systematic increase in density is primarily attributed to the aforementioned adherence of powder particles and slight oversintering effects, effectively increasing the material volume within the bounding box. Fig. 11(b) further illustrates this discrepancy in terms of volume difference and highlights the significant surface area inherent in these lattice designs, which exacerbates the impact of surface roughness and powder adhesion on the final density. These geometric deviations underscore the importance of accounting for manufacturing effects when predicting or analyzing the performance of additively manufactured lattice structures.

3.2. Compressive test results

The compressive mechanical behavior was thoroughly investigated through both quasi-static and dynamic tests.

3.2.1. Quasi-static stress–strain response

The nominal stress–strain curves obtained from quasi-static compression tests are presented in Fig. 12 for both Lat1 N and Lat1 S configurations across the three target relative densities (5%, 10%, and 15%). All curves exhibit the characteristic three-stage response typical of metallic cellular materials: an initial linear elastic region, followed by an extended plastic plateau region where deformation occurs at relatively constant stress, and finally, a densification region marked by a rapid increase in stress as the collapsed cell walls make contact. The plateau region is crucial for energy absorption applications.

As expected, increasing the relative density leads to a significant enhancement in the overall stress levels (stiffness, yield strength, and plateau stress) for both configurations. Comparing the two designs, the modified Lat1 S configuration (larger stuffer, smaller tendon) generally demonstrates enhanced performance. At 5% and 10% relative densities, Lat1 S exhibits a slightly delayed onset of yielding (yield point shifted to approximately 1.5% higher strain compared to Lat1 N) and a correspondingly extended plateau phase, suggesting improved resistance to initial plastic collapse. At the highest density (15%), Lat1 S consistently sustains higher stress levels throughout the entire deformation process compared to Lat1 N, confirming its superior load-bearing capacity. This improved performance, especially at higher relative densities, is attributed to the larger stuffers facilitating a more effective and uniform

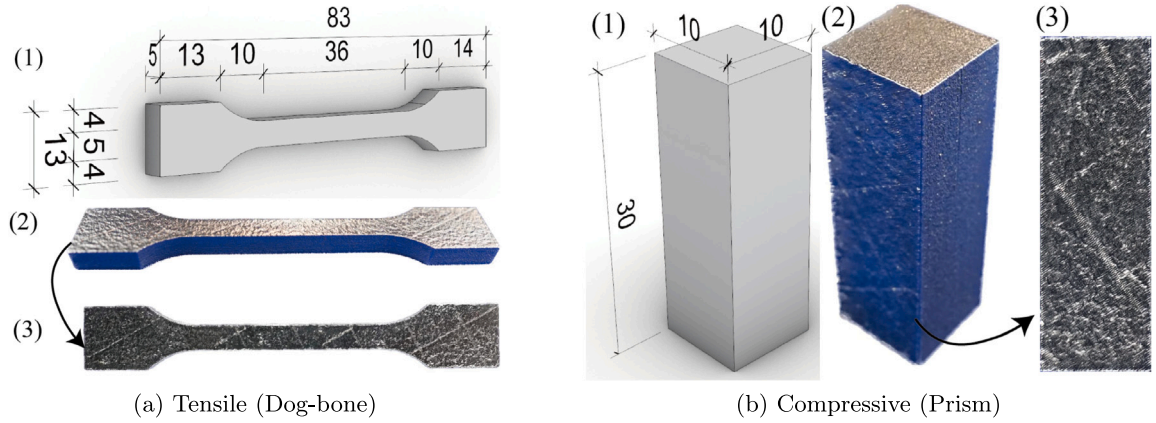

(a) Tensile (Dog-bone) (b) Compressive (Prism)

Fig. 8. Specimens used for base material characterization of SLM-fabricated 316L stainless steel. Each subfigure shows (1) geometry and dimensions, (2) photograph of the printed specimen, and (3) surface detail. (a) Dog-bone specimen for tensile testing. (b) Prism specimen for compression testing. Units: mm.

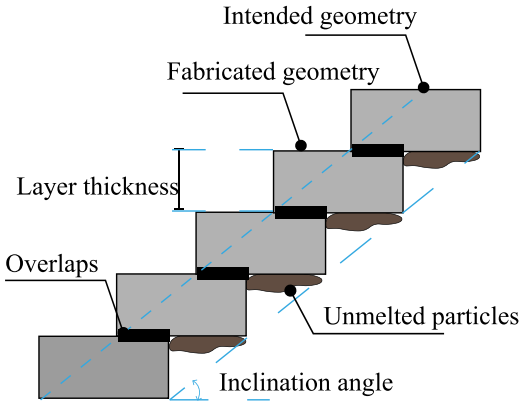

Fig. 9. Illustration of the staircase effect inherent in layer-based additive manufacturing, leading to geometric deviations between the intended (CAD) and fabricated geometry.

load distribution within the lattice, coupled with a dominant stiffening effect that becomes more pronounced as the overall material volume increases. These observations highlight the effectiveness of strategically modifying the stuffer–tendon geometry ratio to improve the mechanical performance of these auxetic lattices.

The plastic plateau region in these stretch-dominated double-arrowhead structures is characterized by noticeable stress fluctuations or oscillations. This behavior is typical for stretch-dominated lattices and arises from the sequential yielding, buckling, and fracture of individual struts, primarily those loaded in tension during the auxetic deformation mechanism [8,37]. As the lattice progressively collapses, these periodic failure events manifest as oscillations in the measured load [1,77]. The magnitude and frequency of these fluctuations can be influenced by manufacturing imperfections and the interplay between different local failure modes (e.g., strut bending vs. buckling). Eventually, significant self-contact between collapsed elements restricts further deformation, leading to the onset of densification and the sharp stress increase.

Further quantification of the quasi-static mechanical performance is provided by the effective elastic modulus and plateau stress, shown as functions of relative density in Figs. 13 and 14, respectively. The elastic modulus (Fig. 13) clearly increases with relative density for both configurations, consistent with cellular mechanics principles. At the lower densities (5% and 10%), the baseline Lat1 N configuration exhibits a slightly higher modulus (647.9 MPa and 1172.0 MPa, respectively) compared to Lat1 S (548.9 MPa and 1031.1 MPa). This suggests greater initial stiffness for the Lat1 N design at lower densities. However, at 15% relative density, the modulus of Lat1 S (1462.1 MPa) becomes comparable to, and even slightly exceeds, that of Lat1 N (1443.2 MPa). This indicates that the stiffening effect of the larger stuffers in Lat1 S becomes more dominant at higher densities, as the increased material volume allows for more direct load transfer and reduced localized deformation in the tendons. The measured moduli (0.65–1.5 GPa) fall within the typical range (0.1–4 GPa) reported for metallic open-cell lattices [1,75].

The yield stress (first peak or 0.2% offset) and plateau stress (averaged over $\varepsilon_{N,S} \approx \varepsilon_{N,Y}$ to $\varepsilon_{N,E} \approx \varepsilon_{N,D}$) are presented in Fig. 14. Both yield and plateau stresses increase substantially with relative density. The Lat1 S configuration consistently exhibits higher plateau stress values than Lat1 N across all densities, particularly evident when considering the average stress over extended strain ranges (e.g., up to 45%). For instance, at $\rho_R = 15\%$, the plateau stress sustained by Lat1 S approaches 70 MPa in the later stages of the plateau, compared to around 65 MPa for Lat1 N, indicating superior load-carrying capacity during large deformations. Both configurations show a slight decrease in stress after the initial yield peak (strain softening), particularly at lower densities, before the stress potentially stabilizes or slightly increases prior to densification. The observed plateau stresses (0.1–70 MPa) are also consistent with literature values (6–60 MPa) for similar materials [1,75], confirming the competitive performance of these auxetic designs, with Lat1 S showing clear advantages at higher densities.

3.2.2. Quasi-static energy absorption

The energy absorption characteristics under quasi-static loading were evaluated using the metrics defined in Section 2.5.2. Fig. 15 plots the energy absorption per unit volume (W, Eq. (9)) and the energy absorption efficiency (η, Eq. (10)) as functions of nominal strain for the different configurations and densities. The densification strain ($\varepsilon_{N,D}$), identified by the peak in the efficiency curve, marks the limit of effective energy absorption. At 5% relative density, Lat1 S achieves a higher densification strain (31.54%) and slightly better peak efficiency (0.32) compared to Lat1 N ($\varepsilon_{N,D} = 27.58\%, \eta_{max} = 0.31$). This trend persists at 10% density, where Lat1 S shows $\varepsilon_{N,D} = 35.15\%$ and $\eta_{max} = 0.34$, outperforming Lat1 N ($\varepsilon_{N,D} = 31.02\%, \eta_{max} = 0.29$). This demonstrates that the modified geometry not only enhances efficiency but also extends the useful deformation range before densification. At 15% relative density, both configurations reach a similar peak efficiency of around 0.27 at $\varepsilon_{N,D} \approx 27\%$. The overall decrease in peak efficiency with increasing density is consistent with observations in other cellular materials, suggesting a trade-off between strength and absorption efficiency at higher densities [74,78].

In terms of total energy absorbed up to densification ($W(\varepsilon_{N,D})$), the Lat1 S configuration consistently outperforms Lat1 N. At 5% density, Lat1 S absorbs 1.74 MJ/m^3, approximately 15% more than Lat1 N

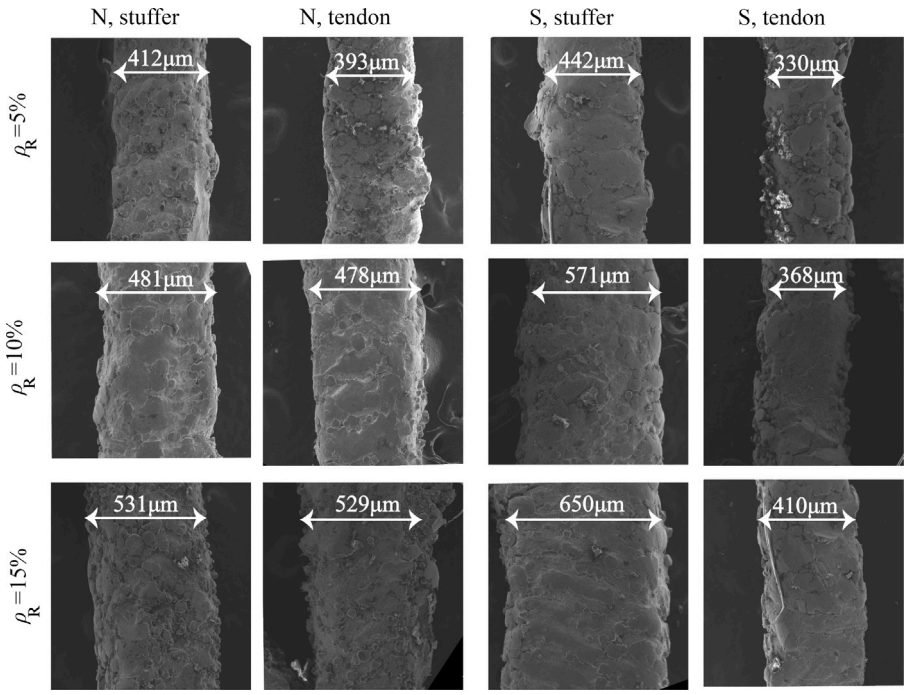

Fig. 10. Representative Scanning Electron Microscopy (SEM) images illustrating the surface morphology and strut quality of the SLM-fabricated 316L stainless steel lattice specimens.

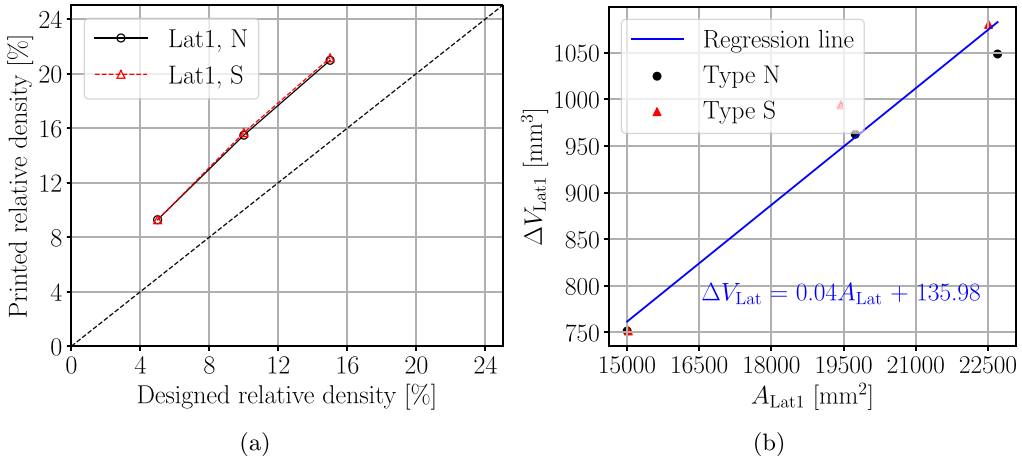

Fig. 11. Quantification of manufacturing discrepancies. (a) Comparison between designed (ρ_R) and measured printed (ρ_{PR}) relative densities for Lat1 N and Lat1 S structures. (b) Percentage volume difference between printed specimens and CAD designs, alongside the designed surface area for each configuration and density.

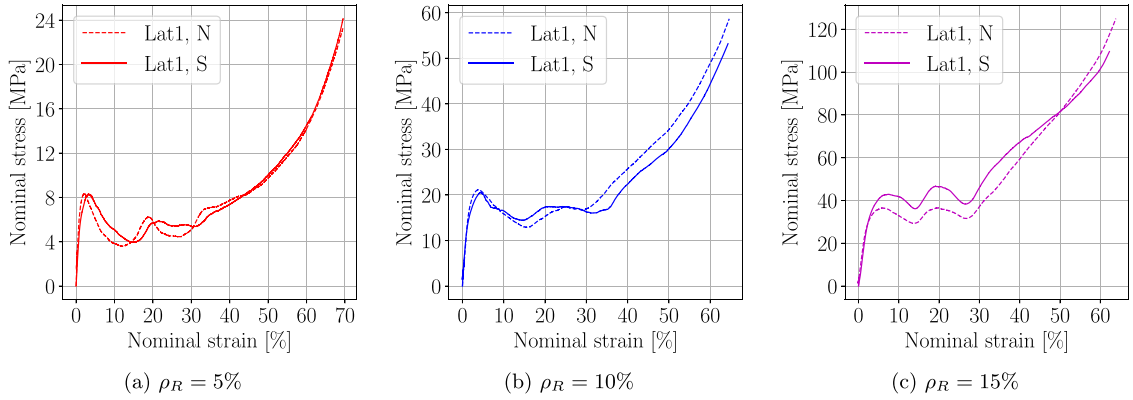

Fig. 12. Experimental quasi-static compressive nominal stress–strain curves for Lat1 N (baseline) and Lat1 S (modified) configurations at target relative densities of (a) 5%, (b) 10%, and (c) 15%.

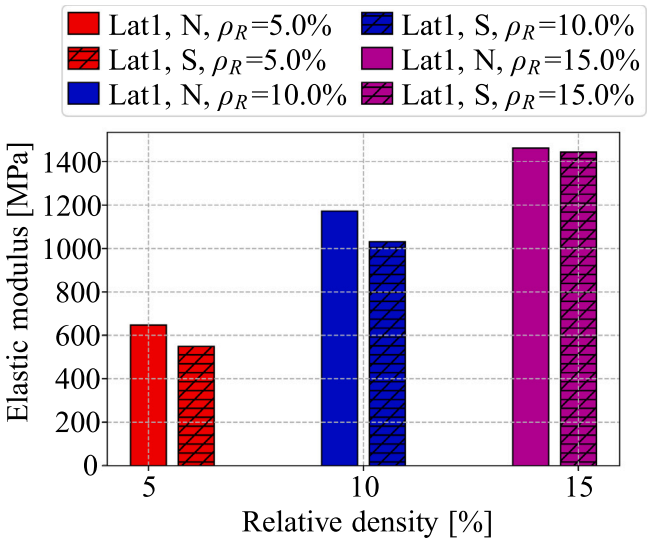

Fig. 13. Variation of effective elastic modulus with measured relative density for Lat1 N and Lat1 S structures under quasi-static compression.

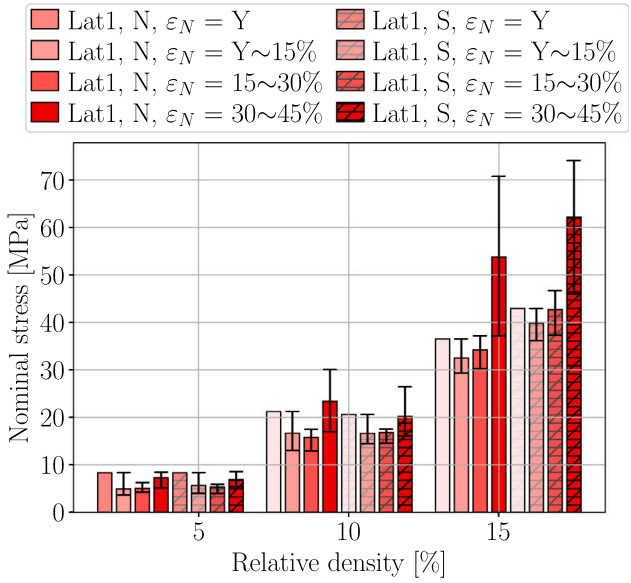

Fig. 14. Quasi-static plateau stress (averaged over the indicated strain ranges, see Fig. 6) as a function of measured relative density for Lat1 N and Lat1 S structures. Error bars represent the maximum and minimum stress within the averaging interval; bars represent the average value.

(1.41 MJ/m^3). This advantage increases with density: at 10%, Lat1 S absorbs 5.80 MJ/m^3 (15.5% higher than Lat1 N's 5.02 MJ/m^3), and at 15%, it reaches 10.67 MJ/m^3, a significant 20% improvement over Lat1 N (8.92 MJ/m^3). This clearly indicates the superior energy dissipation capability of the Lat1 S design, especially at higher relative densities.

The Specific Energy Absorption (SEA, Eq. (11)), which normalizes energy absorption by mass, is plotted against relative density in Fig. 16 for different strain levels within the plateau. At lower densities (5% and 10%), the SEA values for Lat1 N and Lat1 S are comparable. However, at 15% relative density, Lat1 S demonstrates significantly higher SEA, achieving values over 6.42 J/g (approximately 20% higher than Lat1 N) across the strain range from yield up to 30%. This confirms that the mass efficiency of energy absorption for the modified design becomes superior as density increases. The calculated SEA values (3–11 J/g in the plateau) are comparable to those reported for other metallic lattices (e.g., 6.05–10.18 J/g at 35% strain for ρ_R = 30% [69]), validating the effectiveness of these auxetic structures.

Collectively, the energy absorption analysis reveals that the larger stuffer design (Lat1 S) significantly enhances energy dissipation (W) and improves mass efficiency (SEA) at higher relative densities, while also extending the effective deformation range ($\varepsilon_{N,D}$) at lower and intermediate densities.

3.2.3. Dynamic compression via SHPB

The dynamic compressive response was investigated using the SHPB apparatus. Table 3 summarizes the key time-history data obtained from representative tests on Lat1 N and Lat1 S structures at different relative densities (ρ_R = 5%, 10%, 15%) and impact pressures (P = 0.15 MPa and P = 0.25 MPa). The plots show the evolution of strain rate, strain, and stress (calculated using 1D, 2D, and 3D wave analyses) over time.

Analysis of the strain rate versus time plots confirms that, following an initial ramp-up period, a relatively constant strain rate was achieved for a significant duration in most tests, typically stabilizing after approximately 75 µs. This period of constant strain rate, crucial for valid SHPB analysis [59,62], extended for roughly 370 µs based on wave transit calculations (Eqs. (3), (4)). The strain versus time plots show the corresponding accumulation of deformation during the impact event. The stress versus strain plots, derived using the 1D, 2D, and 3D analyses (Eqs. (1a)–(1c)), reveal the dynamic mechanical response. At the lowest density (ρ_R = 5%), significant differences are observed between the 1D, 2D, and 3D stress calculations, particularly in the plateau region, suggesting that stress equilibrium might be less perfectly achieved or that wave propagation effects are more pronounced. As the relative density increases to 10% and 15%, the discrepancy between the different stress calculation methods diminishes notably (e.g., below 11% difference at 15% density), indicating a more uniform stress distribution and better attainment of equilibrium in the denser structures. Increasing the impact pressure (P = 0.15 to 0.25 MPa) consistently leads to higher achieved strain rates and higher stress levels across all densities and configurations.

The Average Strain Rate (ASR, calculated using Eq. (2) over the stable region) achieved during the tests is presented in Table 4. A clear trend emerges: increasing the relative density leads to a lower ASR for a given impact pressure. For instance, at P = 0.15 MPa, the ASR decreases by up to 47% as ρ_R increases from 5% to 15%. Similarly, at P = 0.25 MPa, the reduction is up to 25%. This inverse relationship is expected, as denser structures offer greater resistance to deformation, resulting in a slower rate of strain accumulation under the same impact energy input. At P = 0.25 MPa, the ASR reached values exceeding 500 s^{-1} for the 5% density specimens, decreasing to around 400 s^{-1} for the 15% density specimens.

3.2.4. Dynamic mechanical properties and strain rate sensitivity

The effect of high strain rates on mechanical properties is directly assessed by comparing the dynamic stress–strain curves (Fig. 17, derived from 3D analysis) with the quasi-static curves. Across all relative densities and for both Lat1 N and Lat1 S configurations, the dynamic curves exhibit significantly higher yield stresses and plateau stresses compared to their quasi-static counterparts. For example, at ρ_R = 15%, the yield stress for Lat1 S increases from 42.49 MPa (quasi-static) to 48.98 MPa (dynamic at P = 0.25 MPa, $ASR \approx$ 392 s^{-1}). Similarly, for Lat1 N at 15% density, the yield stress increases from 36.5 MPa to 41.24 MPa ($ASR \approx$ 439 s^{-1}). This pronounced elevation in stress levels under dynamic loading clearly demonstrates the strain-rate sensitivity of these SLM 316L auxetic structures.

Comparing the two configurations under dynamic loading, Lat1 S shows slightly lower dynamic yield stresses than Lat1 N at 5% and 10% densities (by ∼10%–15%). However, at 15% relative density, Lat1 S exhibits a higher dynamic yield stress (by ∼13%) and maintains higher stress levels throughout the measured dynamic strain range compared

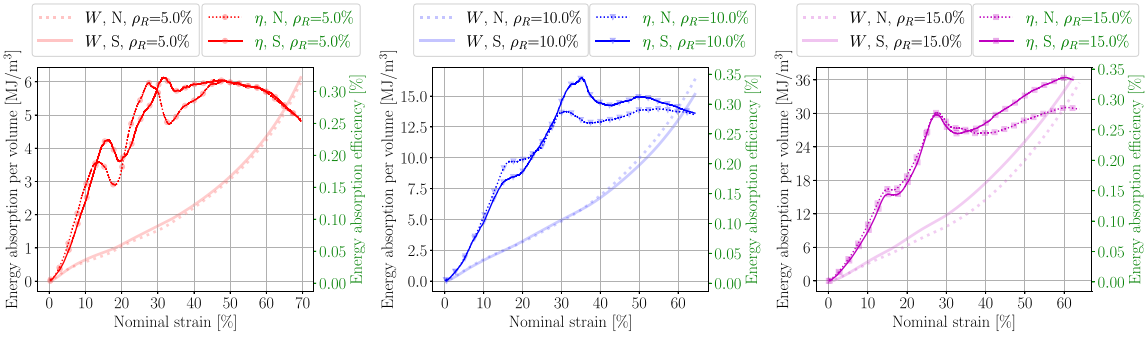

(a) $\rho_R = 5\%$ (b) $\rho_R = 10\%$ (c) $\rho_R = 15\%$

Fig. 15. Quasi-static energy absorption per volume (W) and energy absorption efficiency (η) versus nominal strain for Lat1 N and Lat1 S at target relative densities of (a) 5%, (b) 10%, and (c) 15%.

Table 3
Representative SHPB test results showing time histories of strain rate, strain, and stress (1D, 2D, 3D analyses) for Lat1 structures at different relative densities (ρ_R).

ρ_R	Strain Rate vs Time	Strain vs Time	Stress vs Strain
	N, P=0.15 S, P=0.15 N, P=0.25 S, P=0.25	$\varepsilon_{N,i}$, N, P=0.15 $\varepsilon_{N,r}$, N, P=0.15 $\varepsilon_{N,t}$, N, P=0.15 $\varepsilon_{N,i}$, S, P=0.15 $\varepsilon_{N,r}$, S, P=0.15 $\varepsilon_{N,t}$, S, P=0.15 $\varepsilon_{N,i}$, N, P=0.25 $\varepsilon_{N,r}$, N, P=0.25 $\varepsilon_{N,t}$, N, P=0.25 $\varepsilon_{N,i}$, S, P=0.25 $\varepsilon_{N,r}$, S, P=0.25 $\varepsilon_{N,t}$, S, P=0.25	$\sigma_{N,1D}$,N, P=0.15 $\sigma_{N,2D}$,N, P=0.15 $\sigma_{N,3D}$,N, P=0.15 $\sigma_{N,1D}$,S, P=0.15 $\sigma_{N,2D}$,S, P=0.15 $\sigma_{N,3D}$,S, P=0.15 $\sigma_{N,1D}$,N, P=0.25 $\sigma_{N,2D}$,N, P=0.25 $\sigma_{N,3D}$,N, P=0.25 $\sigma_{N,1D}$,S, P=0.25 $\sigma_{N,2D}$,S, P=0.25 $\sigma_{N,3D}$,S, P=0.25
5%	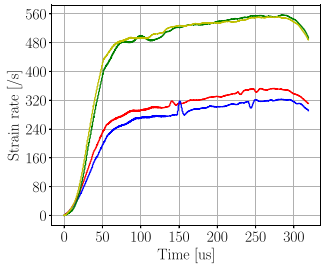	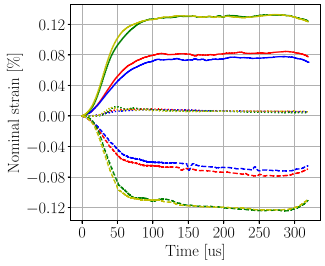	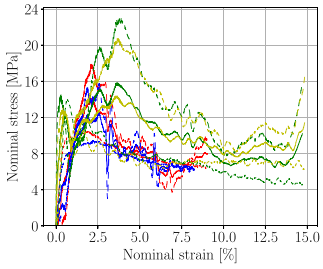
10%	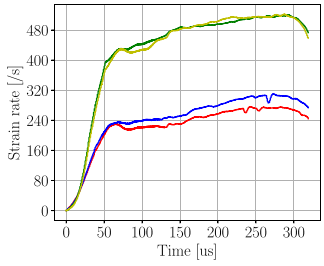	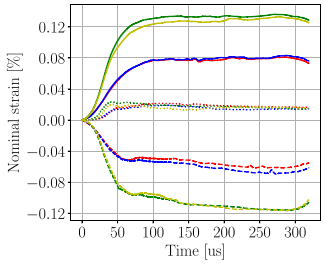	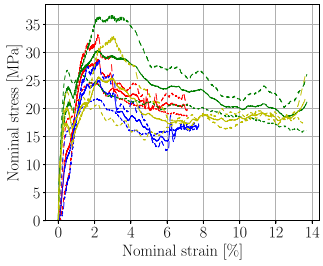
15%	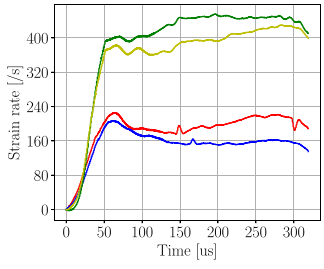	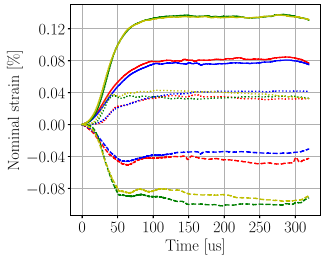	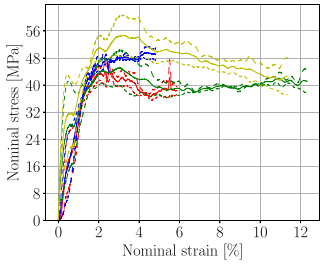

to Lat1 N. This reversal suggests that the structural benefits of the larger stuffers in Lat1 S become particularly advantageous for enhancing strength under high-rate loading conditions at higher densities. The dynamic curves also show more pronounced oscillations than the quasi-static ones, likely due to the interplay of inertia effects and wave propagation phenomena at high strain rates.

The dynamic plateau stress behavior is compared with the quasi-static results in Fig. 18. Consistent with the yield stress observations, the dynamic plateau stresses are significantly higher than the quasi-static ones across all densities and for both configurations. For example, at ρ_R = 15%, the dynamic plateau stress for Lat1 S at P = 0.25 MPa is around 48 MPa, compared to its quasi-static value of 42 MPa. This

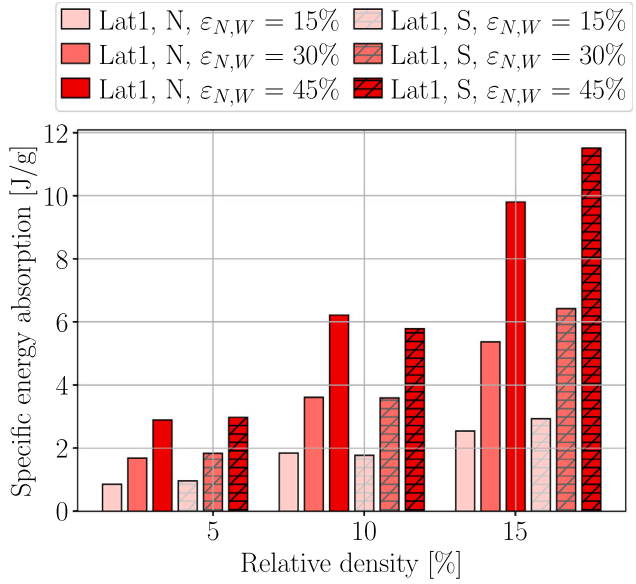

Fig. 16. Specific Energy Absorption (SEA) versus measured relative density under quasi-static compression, evaluated at different nominal strain levels ($\varepsilon_{N,W}$).

Table 4
Average Strain Rate (ASR, in s^{-1}) achieved during dynamic SHPB compression tests for different configurations, relative densities, and impact pressures.

Impact pressure	Config.	ASR (s^{-1})		
(P, MPa)	type	$\rho_R = 5\%$	$\rho_R = 10\%$	$\rho_R = 15\%$
0.15	N	322.41	247.54	194.58
	S	295.27	271.16	157.18
0.25	N	527.67	487.49	439.49
	S	528.31	488.10	391.59

enhancement further underscores the strain-rate sensitivity. The difference between yield stress and subsequent plateau stress (stress drop) appears less pronounced in the dynamic tests compared to quasi-static, particularly for the higher density Lat1 S structure, suggesting potentially more stable collapse under dynamic conditions. The Lat1 S configuration again demonstrates superior dynamic plateau stress compared to Lat1 N at 15% density, reinforcing its advantage under high-rate impact at higher densities. The discrepancy between 1D and 3D stress analyses remains more noticeable at lower densities, where the concept of a uniform macroscopic stress state is inherently more challenging to satisfy due to increased local heterogeneity and deformation localization. However, this discrepancy diminishes significantly at 15% density, supporting the idea of more uniform dynamic stress states in denser structures and validating the use of average nominal values for macroscopic characterization.

3.2.5. Dynamic energy absorption properties

The energy absorption performance under dynamic loading is crucial for impact applications. Figs. 19 and 20 compare the dynamic energy absorption metrics (W, η, SEA) with the quasi-static results. Fig. 19 shows W and η versus strain. A key finding is the dramatic increase in energy absorption per volume (W) under dynamic loading compared to quasi-static loading at the same strain level. For example, at $\varepsilon_N = 15\%$, the dynamic W (at $P = 0.25$ MPa) is several times higher than the quasi-static W across all densities. Under dynamic impact at $P = 0.25$ MPa, the structures absorbed significant energy within the limited strain range achievable during the SHPB pulse duration, reaching up to approximately 12 MJ/m^3 (5% density), 30 MJ/m^3 (10% density), and 50 MJ/m^3 (15% density) at the maximum recorded dynamic strain.

Comparing configurations dynamically, Lat1 S shows superior energy absorption (W) compared to Lat1 N at 15% density (by ~25%), although Lat1 N performed slightly better at 10% density under dynamic conditions within the tested strain range. The dynamic energy absorption efficiency (η) also tends to be higher than the quasi-static efficiency at equivalent strains, although the difference is less dramatic than for W. The difference in calculated W between 1D and 3D analyses decreases with increasing density (from 31% at 5% to 3% at 15%), while the efficiency η shows minimal difference between analyses (< 2%) across all conditions.

The dynamic Specific Energy Absorption (SEA) is presented in Fig. 20. Consistent with W, dynamic SEA values are substantially higher than quasi-static values at comparable strains, highlighting enhanced mass–specific energy absorption at high rates. For instance, at $\rho_R = 15\%$ and $\varepsilon_N \approx 5\%$, the dynamic SEA (at $P = 0.25$ MPa) exceeds 14 J/g, roughly 14 times the quasi-static value at that strain. At the maximum dynamic strain achieved, SEA values reached up to 32 J/g for Lat1 S at 15% density, compared to 28 J/g for Lat1 N. While Lat1 N showed slightly higher dynamic SEA at lower densities (5%, 10%) within the limited strain range, Lat1 S demonstrated superior performance at the highest density (15%). The difference between 1D and 3D SEA calculations is again more pronounced at lower densities, converging at higher densities. These results confirm the significant enhancement in energy absorption capacity under dynamic loading and reinforce the advantage of the Lat1 S configuration at higher relative densities for impact applications.

3.2.6. Poisson's ratio under different conditions

The evolution of the nominal Poisson's ratio (ν_N, calculated from DIC using Eq. (12)) during quasi-static compression is shown in Fig. 21 as a function of nominal strain for both configurations across the three relative densities. (Note: Dynamic Poisson's ratio was not reliably extracted from high-speed imaging in this study, so the plot focuses on quasi-static results and implies dynamic trends based on deformation observations). All tested structures exhibited auxetic behavior (negative Poisson's ratio) during the initial stages of compression.

Several key trends are evident. Firstly, the magnitude of the negative Poisson's ratio generally decreases (becomes less negative) as the relative density increases. At 5% density, Lat1 N reaches ν_N values below −1.0, indicating strong auxetic response, consistent with literature values for similar 3D auxetics [37]. At 15% density, the minimum ν_N is closer to −0.75, indicating reduced lateral contraction relative to axial compression. This suggests that denser structures are inherently stiffer and resist the auxetic deformation mechanism more strongly.

Secondly, comparing the two configurations, at lower densities (5% and 10%), the baseline Lat1 N exhibits a more negative Poisson's ratio (stronger auxetic effect) than Lat1 S during the initial strain regime (up to ~1.5%–2% strain). This suggests Lat1 N deforms more readily via the auxetic mechanism at low strains when density is low. However, at the highest density (15%), this trend reverses slightly, with Lat1 S showing a marginally more negative ν_N than Lat1 N initially. The overall evolution of ν_N with increasing strain is complex, often showing an initial decrease to a minimum value followed by an increase as deformation progresses and different mechanisms (e.g., buckling, contact) become active. The DIC deformation maps provided in Appendix A offer further visual insight into the lateral and axial deformation patterns underlying these Poisson's ratio trends. Observations from dynamic tests (though not quantified for ν_N) suggest that higher strain rates tend to suppress lateral deformation compared to quasi-static loading, leading to less negative effective Poisson's ratios, particularly at lower densities where inertia effects might be more significant relative to structural stiffness.

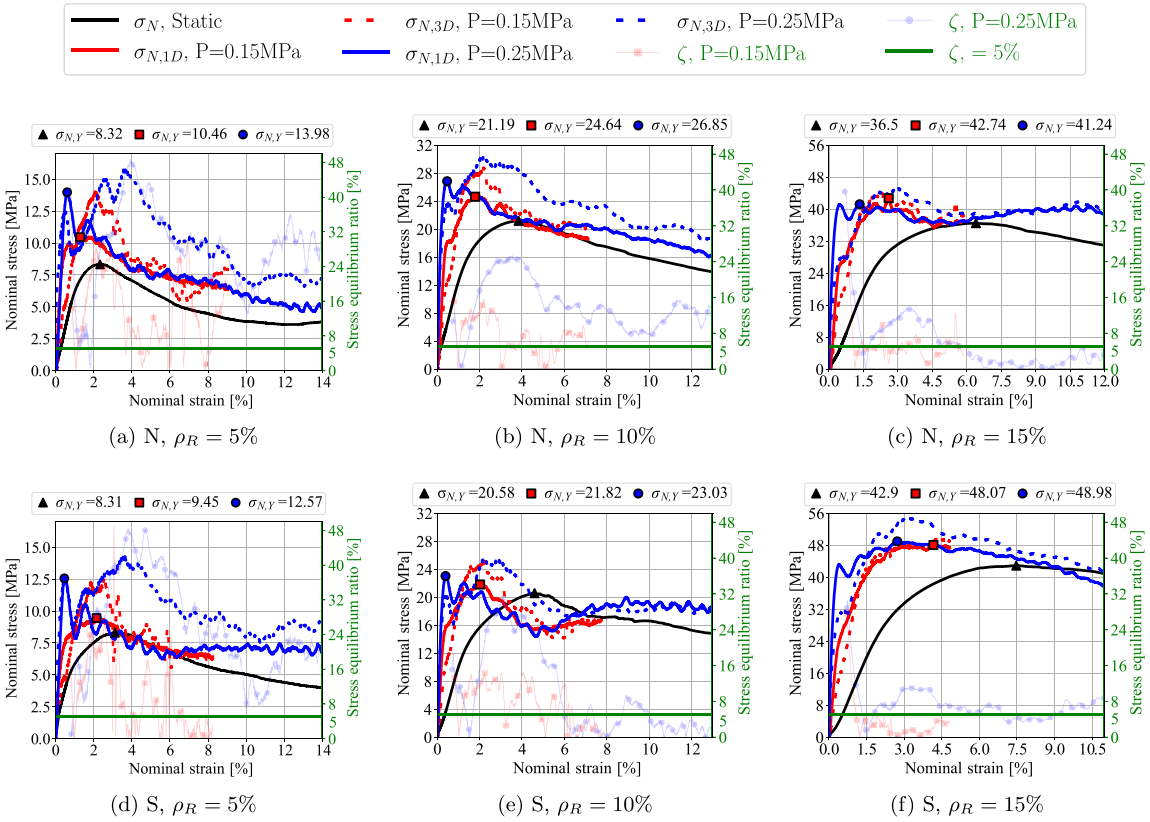

Fig. 17. Comparison of quasi-static (black solid) and dynamic SHPB (colored dashed/dotted, 3D analysis) nominal stress–strain curves for Lat1 N (a–c) and Lat1 S (d–f) configurations at target relative densities of 5%, 10%, and 15%. Dynamic tests performed at impact pressures $P = 0.15$ and 0.25 MPa.

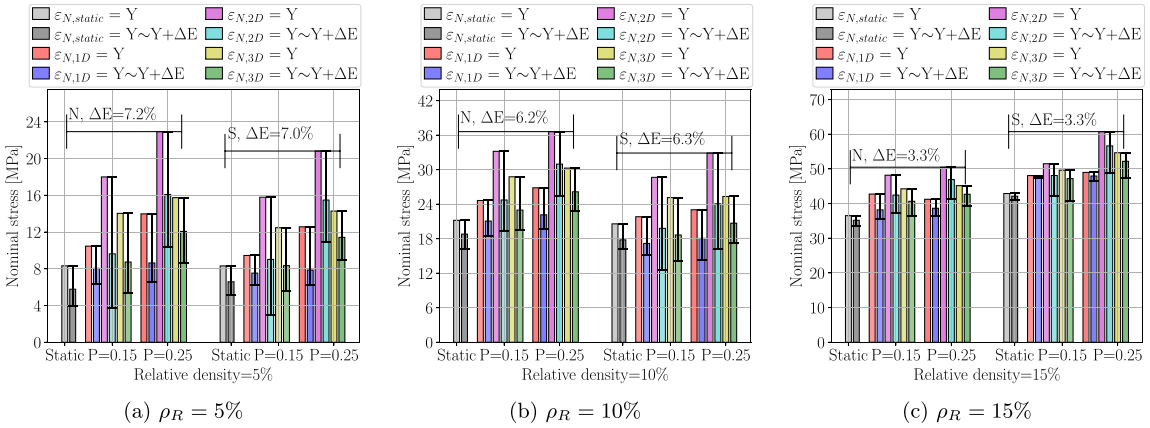

Fig. 18. Comparison of quasi-static (gray bars) and dynamic (colored bars, 3D analysis) plateau stresses for Lat1 N and Lat1 S across different relative densities: (a) 5%, (b) 10%, (c) 15%. Stresses averaged over strain ranges near yield ($\varepsilon_{N,S} = Y$) and extended plateau ($Y \sim Y + \Delta E$). Error bars show max/min stress in interval.

4. Numerical simulations

To complement the experimental investigation and gain deeper insights into the deformation mechanisms, Finite Element Method (FEM) simulations were performed using the commercial software ABAQUS/Explicit. This section details the development and validation of the material model and the subsequent comparison of simulation results with experimental data for the lattice structures.

4.1. Material model development and validation

Accurate prediction of the mechanical response of the auxetic lattice structures via FEM necessitates a reliable constitutive model for the base material, SLM-fabricated 316L stainless steel. The required material parameters were derived from the experimental tensile and compressive tests performed on solid dog-bone and prism specimens, respectively, as described in Section 2.6. The base material properties

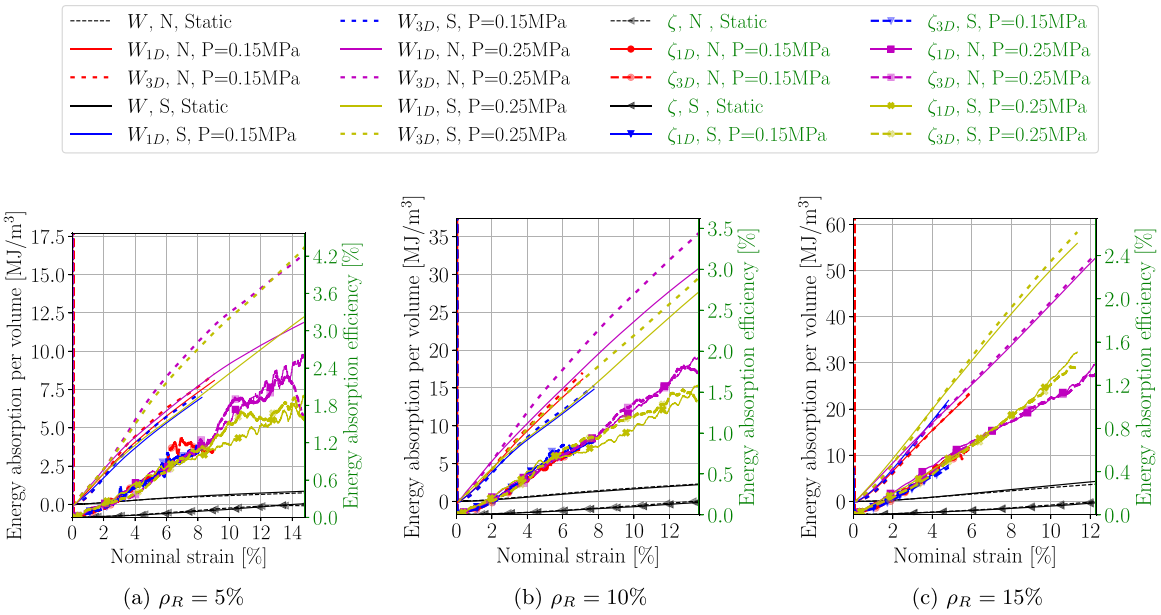

Fig. 19. Comparison of quasi-static and dynamic energy absorption per volume (W) and efficiency (η) versus nominal strain for Lat1 N and Lat1 S at target relative densities of (a) 5%, (b) 10%, and (c) 15%. Dynamic results shown for 1D and 3D analyses at $P = 0.15$ and 0.25 MPa.

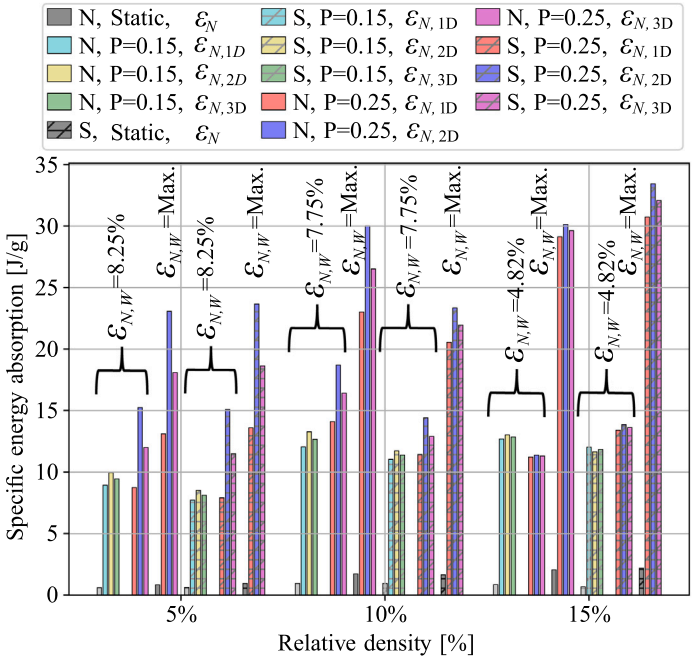

Fig. 20. Comparison of quasi-static and dynamic Specific Energy Absorption (SEA) versus measured relative density, evaluated at different nominal strain levels. Dynamic results shown for 1D, 2D, and 3D analyses at $P = 0.15$ and 0.25 MPa.

determined were: density $\rho_{\text{solid}} = 7800\,\text{kg/m}^3$, Young's Modulus $E = 193\,\text{GPa}$, and quasi-static yield stress $\sigma_Y \approx 390\,\text{MPa}$. To capture the complex elasto-plastic behavior, including strain hardening, strain rate sensitivity, and potential failure, the Johnson–Cook (JC) constitutive model and failure criterion were employed [79].

The JC strength model describes the flow stress σ as a function of equivalent plastic strain (ε_{ep}), plastic strain rate ($\dot{\varepsilon}$), and temperature (T):

$$\sigma = (A + B\varepsilon_{ep}^{n})(1 + C\ln\dot{\varepsilon}^{*})(1 - T^{*m}) \tag{13}$$

where A is the quasi-static yield stress, B and n are strain hardening parameters, C governs strain rate sensitivity, and m accounts for thermal softening. $\dot{\varepsilon}^{*} = \dot{\varepsilon}/\dot{\varepsilon}_0$ is the dimensionless plastic strain rate relative to a reference strain rate $\dot{\varepsilon}_0$ (typically $1\,\text{s}^{-1}$), and $T* = (T - T_0)/(T_m - T_0)$ is the homologous temperature relative to the room temperature T_0 and melting temperature T_m. Since the experiments were conducted under nearly isothermal conditions (especially quasi-static), and temperature rise during dynamic tests was assumed to have a secondary effect compared to strain rate for these conditions, the thermal softening term $(1 - T^{*m})$ was simplified by setting $T^{*} = 0$ (i.e., m was not explicitly fitted or used). The parameters A, B, C, and n were determined by fitting Eq. (13) (without the temperature term) to the stress–strain data obtained from the quasi-static tension and compression tests (providing A, B, n) and considering the dynamic enhancement observed in the

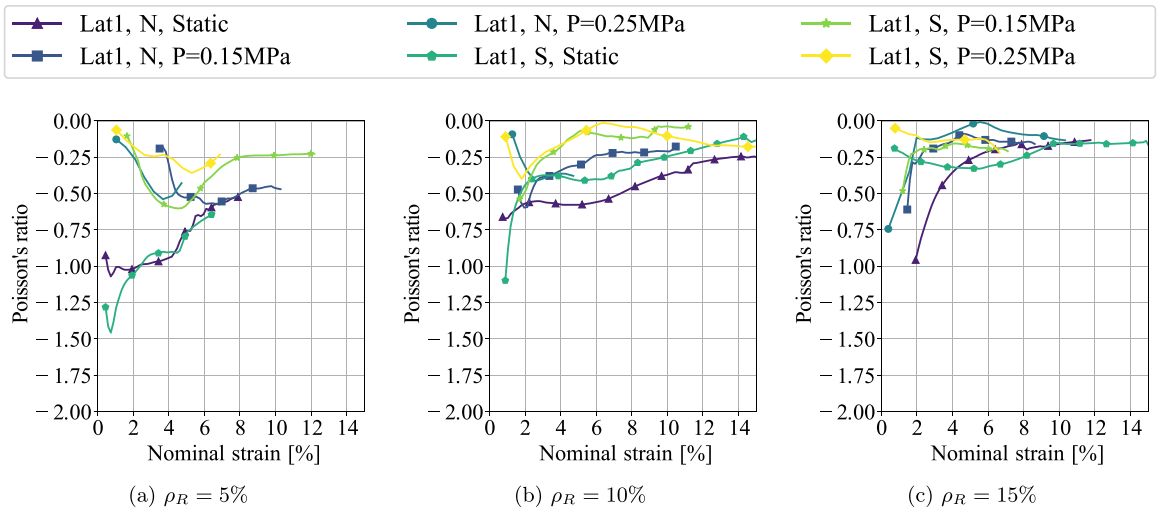

Fig. 21. Evolution of quasi-static nominal Poisson's ratio (ν_N) as a function of nominal strain for Lat1 N and Lat1 S configurations at target relative densities of (a) 5%, (b) 10%, and (c) 15%, calculated from DIC measurements.

Table 5
Johnson–Cook (JC) strength model parameters for SLM 316L stainless steel from this study and selected literature sources.

Reference	A (MPa)	B (MPa)	C (-)	n (-)	m (-)
Li [80]	380	825	0.115	0.73	1.0[a]
Platek et al. [81]	542	303	0.028	0.29	1.0[a]
Sandmann et al. [82]	545	821	0.010	0.70	1.0[a]
Xue et al. [83]	489	554	0.039	0.60	1.0[a]
Alkhatib et al. [84]	595	1635	0.011	0.98	1.0[a]
This study	**390**	**1277**	**0.011**	**0.74**	N/A

[a] Literature values for m might vary or be assumed if not provided; N/A: Not Applicable/Used.

lattice tests to estimate C. The resulting parameters for this study are listed in Table 5, alongside values reported in literature for SLM 316L for comparison. Fig. 22 illustrates the fitted model's prediction compared to literature models, highlighting the significant strain rate sensitivity captured, which is crucial for dynamic simulations. It is recognized that SLM-fabricated materials can exhibit anisotropic properties due to the layer-wise deposition and solidification processes. In this study, the Johnson–Cook model was calibrated using tensile and compressive tests on solid specimens fabricated under the same SLM conditions and oriented to reflect the principal loading direction experienced by the lattice structures (axial compression). While the model itself is isotropic, the parameters derived implicitly account for the effective material response in the tested direction. For future studies requiring highly detailed microstructural-level analysis of anisotropy, more complex anisotropic constitutive models could be considered.

To simulate potential material failure within the lattice struts, particularly under large deformations, the JC failure model was also incorporated [85]. This model defines the equivalent plastic strain at failure (ε_f) as:

$$\varepsilon_f = [D_1 + D_2 \exp(D_3 \sigma^*)][1 + D_4 \ln \dot{\varepsilon}^*][1 + D_5 T^*] \tag{14}$$

where D_1 to D_5 are material failure constants. The model accounts for the influence of stress triaxiality ($\sigma^* = p/q$, where p is hydrostatic pressure and q is von Mises stress), strain rate ($\dot{\varepsilon}^*$), and temperature (T^*) on ductility. Initial values for the failure parameters (D_1 to D_5) were adopted from literature sources investigating fracture in SLM 316L [86,87]. These parameters were then iteratively adjusted by comparing the predicted failure initiation and propagation in the simulations with observations from the experimental tests (e.g., strut fracture patterns) until a reasonable qualitative match was achieved. The final parameters used in the simulations were: $D_1 = 0.2$, $D_2 = 1.5$, $D_3 = 0.5$, $D_4 = 0.09$, and $D_5 = 0.5$. (Again, the temperature term $1 + D_5 T^*$ was effectively deactivated by assuming $T^* = 0$).

The validity of the calibrated JC strength model was confirmed by simulating the quasi-static tensile (dog-bone) and compressive (prism) tests used for characterization. Fig. 23 overlays the FEM-predicted stress–strain curves with the experimental results. The close agreement observed for both loading conditions demonstrates the model's capability to accurately reproduce the base material's constitutive response, including yield, strain hardening, and the tension–compression asymmetry typical of some metals.

Furthermore, the model's ability to predict localized deformation and failure initiation was assessed by comparing the strain fields predicted by FEM during the tensile test simulation with those measured experimentally using DIC. Fig. 24 shows the experimental strain distribution maps at different stages of loading, clearly illustrating strain localization and necking prior to fracture. Fig. 25 presents the corresponding equivalent plastic strain (PEEQ) contours predicted by the FEM simulation. The strong qualitative agreement in the location and pattern of strain concentration provides confidence in the model's ability to capture realistic deformation behavior, including failure precursors.

In summary, the comprehensive comparison between experimental results and numerical predictions for the base material tests demonstrates a high degree of correlation. This validates the robustness of the calibrated Johnson–Cook strength and failure models for accurately representing the mechanical behavior of the SLM-fabricated 316L stainless steel. This validated constitutive model was subsequently used in the FEM simulations of the auxetic lattice structures.

4.2. Simulation of lattice structures and comparison with experiments

FEM simulations of the Lat1 N and Lat1 S auxetic lattice structures under both quasi-static and dynamic compression were conducted to compare directly with the experimental findings. The geometry for the FEM models (Fig. 26) was based on the CAD designs but crucially adjusted to match the *measured* as-printed relative densities (ρ_{PR}) of approximately 9%, 16%, and 21% (corresponding to the target ρ_R of $5\%, 10\%, 15\%$, respectively). This step is essential for meaningful comparison, as modeling the ideal CAD geometry without accounting for manufacturing deviations can lead to significant discrepancies [88].

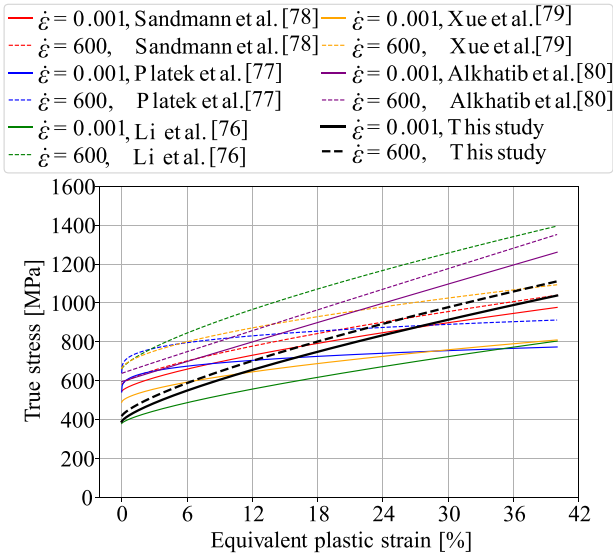

Fig. 22. Comparison of the Johnson–Cook strength model fitted in this study with models proposed in the literature for SLM 316L steel, illustrating strain rate sensitivity.

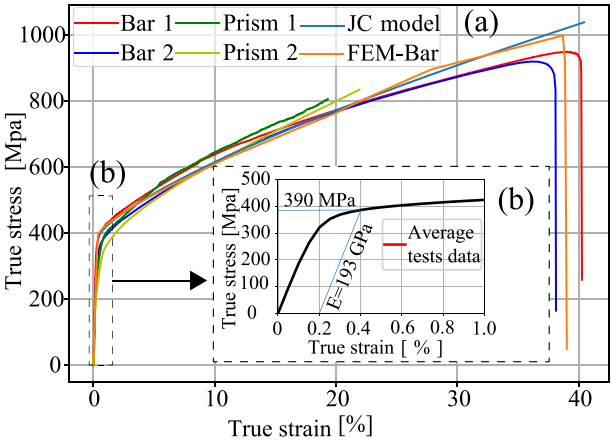

Fig. 23. Validation of the calibrated Johnson–Cook material model: comparison of FEM-simulated stress–strain curves with experimental data from quasi-static tensile (dog-bone) and compressive (prism) tests on SLM 316L steel.

The adjustment involved uniformly scaling the strut thicknesses in the CAD model until the calculated volume matched that derived from the measured ρ_{PR}.

The simulations utilized the validated JC material model described in Section 4.1. The lattice structures were meshed using solid tetrahedral elements (C3D10M in ABAQUS library) after performing a mesh sensitivity study to ensure convergence of the global response. The lattice was placed between two rigid plates representing the loading platens. The bottom plate was fixed in all degrees of freedom. The top plate was constrained to move only vertically, and compressive loading was applied by prescribing a velocity to this plate. For quasi-static simulations, a slow velocity corresponding to the experimental strain rate ($\dot{\varepsilon} \approx 4 \times 10^{-4}\,\mathrm{s}^{-1}$) was applied. For dynamic simulations, velocities were chosen to achieve average strain rates (ASR) matching those measured in the SHPB experiments for each specific configuration, density, and impact pressure (see Table 4). Contact between the lattice surfaces and the rigid plates was defined using a penalty-based algorithm with a friction coefficient of $\mu = 0.1$ to approximate the lubricated experimental conditions. General contact was also defined between lattice surfaces to capture self-contact during densification.

Table 6 presents a direct comparison between the nominal stress–strain curves obtained from FEM simulations and those measured experimentally under both quasi-static and dynamic (SHPB, $P = 0.25$ MPa) conditions. Overall, the FEM results demonstrate strong agreement with the experimental data, particularly for the higher relative densities (10% and 15%, corresponding to $\rho_{PR} \approx 16\%$ and 21%). The simulations accurately capture the elastic stiffness, yield point, plateau stress level, and the onset of densification. At the lowest density (5%, $\rho_{PR} \approx 9\%$), the FEM tends to slightly overestimate the stress levels compared to the experiments. This minor discrepancy might stem from the increased influence of subtle geometric imperfections (like strut waviness or porosity, not explicitly modeled beyond density matching) at lower densities, or challenges in perfectly replicating the complex stress state and boundary conditions of the experiments. Nonetheless, the model successfully captures the key qualitative trends and provides reliable quantitative predictions, especially at moderate to higher densities.

The simulations also replicate the experimental observation that dynamic loading leads to significantly higher stress levels (steeper slopes, higher plateau) compared to quasi-static loading, confirming the model's ability to capture strain rate effects via the JC parameter C. The steeper dynamic slope might also be partly influenced by numerical contact dynamics in the simulation, mirroring potential physical effects at the specimen–platen interface during high-rate tests.

Intriguingly, the FEM simulations also reproduce the difference in stress oscillations observed between the two configurations. Consistent with experiments, the Lat1 S curves (both static and dynamic) exhibit more pronounced oscillations and, notably, show evidence of a secondary stress peak occurring around 20% strain, especially under dynamic loading. This feature, absent or less prominent in the Lat1 N curves, suggests a more complex, potentially multi-stage collapse mechanism in the modified structure, which might contribute to its enhanced energy absorption capacity over extended strains. The FEM effectively captures this difference in mechanical signature, indicating its sensitivity to the geometric modifications.

Quantitatively, the discrepancy between FEM predictions and experimental results for key parameters like plateau stress is generally less than 13%, particularly for the 10% and 15% density cases. This

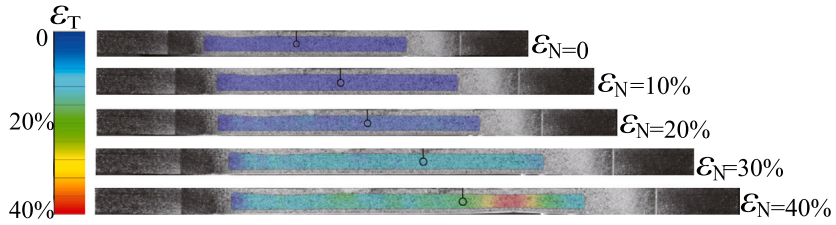

Fig. 24. Experimental strain distribution maps obtained via Digital Image Correlation (DIC) during quasi-static tensile testing of an SLM 316L dog-bone specimen at increasing load levels, showing strain localization in the necking region.

Table 6
Comparison of nominal stress versus nominal strain curves: FEM simulations versus experimental results (quasi-static and dynamic SHPB at $P = 0.25$ MPa) for Lat1 N and Lat1 S configurations at different nominal relative densities.

Configuration	$\rho_R = 5\%$ ($\rho_{PR} \approx 9\%$)	$\rho_R = 10\%$ ($\rho_{PR} \approx 16\%$)	$\rho_R = 15\%$ ($\rho_{PR} \approx 21\%$)
N	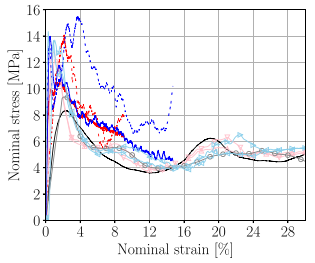	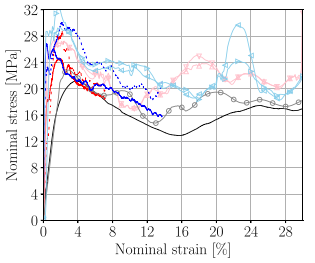	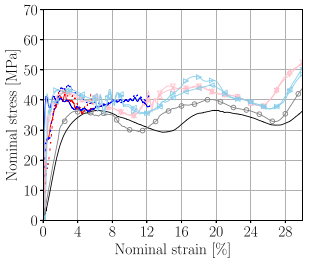
S	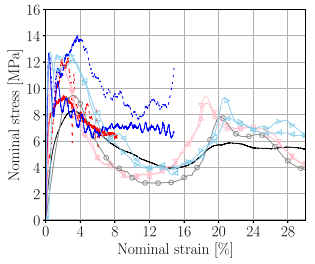	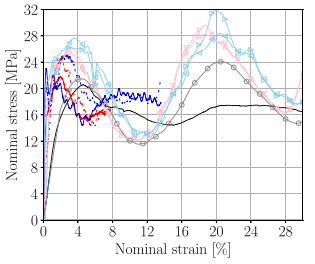	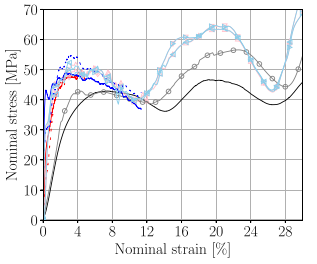

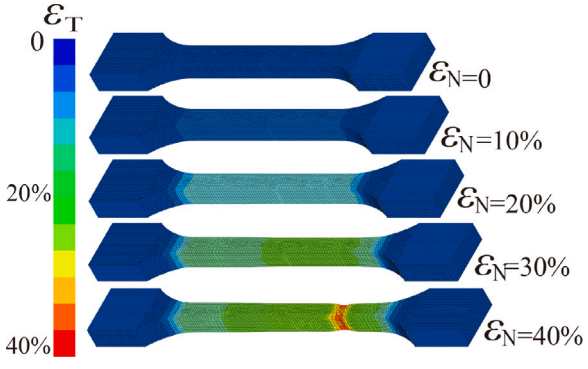

Fig. 25. FEM-predicted equivalent plastic strain (PEEQ) distribution in the dog-bone specimen simulation under tensile loading, corresponding to the stages shown in Fig. 24, illustrating accurate capture of necking.

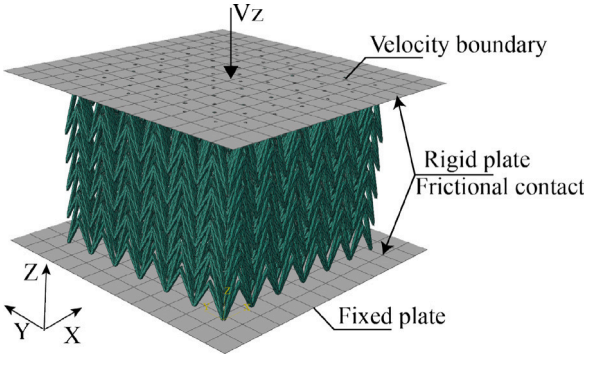

Fig. 26. Finite Element model setup in ABAQUS for the Lat1 auxetic lattice structure under compression between two rigid plates.

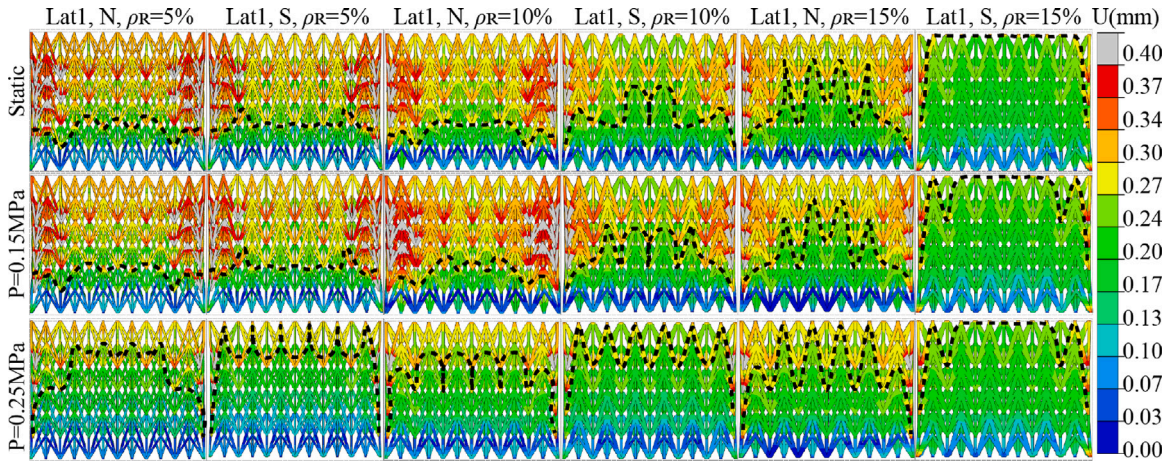

Fig. 27. FEM-predicted deformation distribution (vertical displacement contours) at a nominal strain of $\varepsilon_N = 5\%$ for Lat1 N and Lat1 S structures under quasi-static ($P = 0$) and dynamic ($P = 0.15, 0.25$ MPa) loading across the three relative densities ($\rho_{PR} \approx 9\%, 16\%, 21\%$). Gray box shows initial undeformed outline.

level of agreement is consistent with or better than that reported in similar validation studies for additively manufactured metal lattices under compression [87,89,90].

Fig. 27 provides snapshots of the predicted deformation distribution (displacement contours) from FEM simulations at a nominal strain of $\varepsilon_N = 5\%$ under various conditions. These visualizations reveal differences in deformation patterns. Dynamic loading generally leads to more localized deformation near the impacted (top) end compared to the more uniform deformation under quasi-static loading, particularly at lower densities. The Lat1 S configuration appears to maintain slightly better uniformity compared to Lat1 N under dynamic load, especially at higher densities where Lat1 N shows hints of incipient buckling modes. Increasing the dynamic impact pressure ($P = 0.15$ vs $P = 0.25$ MPa) exacerbates the deformation localization. These visual results complement the stress–strain curves by illustrating how the load is distributed and accommodated spatially within the structures under different conditions.

4.3. Deformation mode analysis

A comparison between the experimentally observed deformation modes (via DIC; see Appendix A, Figs. A.30–A.32) and the numerically predicted ones (via FEM; see Appendix B, Tables B.7–B.9) provides valuable insights into the collapse mechanisms. Under quasi-static loading, both experiments and simulations show a relatively homogeneous, layer-by-layer collapse for both Lat1 N and Lat1 S configurations, particularly in the early stages ($\varepsilon_N \leq 15\%$). However, the DIC results suggest that the Lat1 S structure, with its larger stuffers, maintains this uniformity slightly better, exhibiting more controlled energy dissipation and potentially delaying localized failure compared to Lat1 N. At higher quasi-static strains ($\varepsilon_N > 20\%$), both configurations exhibit some lateral bulging, likely influenced by friction at the platens, which can lead to a less uniform, drum-shaped deformation profile. This effect appears somewhat more pronounced in the Lat1 N DIC results.

Under dynamic SHPB loading, the deformation becomes inherently less uniform due to inertia and wave propagation effects. Experimental high-speed imaging and FEM results (Appendices A and B) indicate that deformation tends to initiate near the impact face and propagate through the structure. Again, the Lat1 S configuration appears to manage this dynamic load more effectively, showing relatively more uniform deformation progression compared to Lat1 N. The baseline Lat1 N exhibits more significant lateral bulging and signs of buckling instability, especially at higher dynamic strains ($\varepsilon_N > 20\%$–30%) and higher densities.

In summary, both experimental observations and numerical simulations confirm that the double-arrowhead lattice exhibits auxetic behavior (initial lateral contraction, visible in DIC maps) followed by a progressive collapse mechanism. The modified Lat1 S geometry consistently demonstrates enhanced structural stability, characterized by reduced lateral deformation and suppressed buckling tendencies, particularly under dynamic loading conditions, compared to the baseline Lat1 N configuration. The FEM simulations successfully capture these distinct deformation modes and corroborate the global stress–strain responses, including localized stress fluctuations observed experimentally. This consistency underscores the critical role of the enlarged stuffers in improving load distribution and enhancing the overall structural integrity and energy absorption performance, validating the effectiveness of this geometric optimization strategy, especially for impact-resistance applications, aligning with findings in related auxetic studies [8,37,91,92].

5. Discussion

This section discusses the key findings regarding strain rate sensitivity and the influence of relative density on the mechanical performance of the auxetic lattice structures.

5.1. Strain rate sensitivity

The dynamic mechanical behavior of the SLM 316L auxetic lattices was significantly influenced by the loading rate, as quantified by the Dynamic Increase Factor (DIF, defined as the ratio of dynamic stress to quasi-static stress at the same strain). Fig. 28 plots the DIF (calculated using plateau stresses) against the average strain rate ($\dot{\varepsilon}$) achieved in the SHPB tests. A clear positive correlation is observed: the DIF increases substantially from approximately 1.15 at lower strain rates ($\dot{\varepsilon} \approx 150\,s^{-1}$) to over 1.85 at higher rates ($\dot{\varepsilon} \approx 500\,s^{-1}$). This demonstrates significant strain-rate sensitivity, indicating enhanced dynamic strength and deformation resistance under rapid loading conditions. This strengthening is primarily attributed to the intrinsic strain-rate sensitivity of the 316L stainless steel base material, although micro-inertial effects within the lattice structure likely also contribute to the dynamic response, especially at higher rates [93]. The observed DIF range (1.15–1.85) aligns well with previous studies on stainless

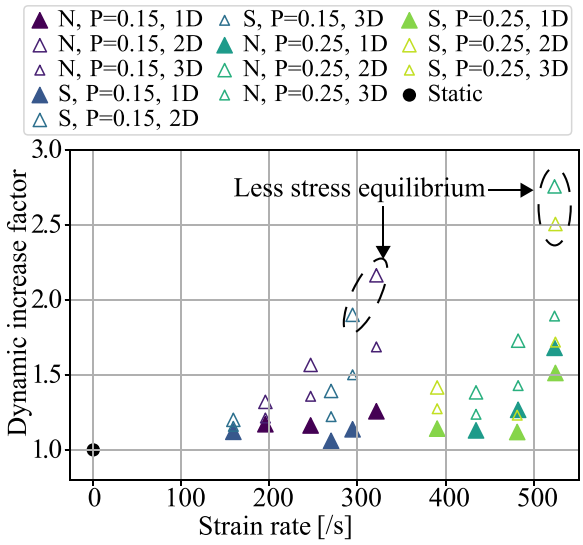

Fig. 28. Dynamic Increase Factor (DIF) calculated from plateau stress versus average strain rate ($\dot{\varepsilon}$) achieved in SHPB tests. Different markers represent DIF calculated using 1D, 2D, and 3D stress analyses. Regions indicating less optimal stress equilibrium ($\zeta(t) > 5\%$) are noted.

steel lattices under similar strain rate regimes (e.g., 1.13–1.76 reported by Li et al. [93] for rates up to 500 s^{-1}), confirming the consistent rate-dependent behavior of these architected materials.

Comparing the DIF values derived from the 1D, 2D, and 3D SHPB analysis methods (representing stress calculations based on transmitted wave only, incident/reflected waves, and all three waves, respectively), the 2D and 3D analyses consistently yield slightly higher DIF values than the 1D analysis. This discrepancy likely arises because the 2D and 3D methods incorporate information about the stress state at the front face of the specimen, which can be influenced by complex wave interactions and reflections, potentially leading to higher calculated average stresses, especially during the dynamic loading phase before perfect equilibrium is established across the entire specimen length.

The plot also highlights data points corresponding to tests where stress equilibrium was less perfectly achieved (relative stress difference $\zeta(t) > 5\%$, see Eq. (5)). These deviations typically occurred at higher strain rates (beyond $\sim$ 300 s^{-1}) and could lead to some variability or artificial inflation of the calculated DIF values due to non-uniform stress distribution within the specimen during the measurement interval. However, the overall trend of increasing DIF with strain rate remains robust. The difference between 1D, 2D, and 3D results, while relatively small, suggests that the more comprehensive 3D analysis potentially captures the complex dynamic stress state slightly more accurately, reflecting the intricate shock wave interactions inherent in high-rate loading of lattice structures.

In essence, the analysis confirms a pronounced strain-rate dependency in the compressive response of these double-arrowhead auxetic lattices. The dynamic deformation resistance significantly increases with loading rate, primarily driven by base material properties. Understanding this sensitivity, along with the nuances revealed by different SHPB analysis methods, is crucial for accurately predicting performance in dynamic applications. The origins of strain-rate sensitivity in lattice materials are generally attributed to a combination of the base material's inherent rate dependency (strain hardening enhancement at higher rates [94,95]) and structural effects related to inertia, where rapid loading hinders the ability of struts to deform and redistribute load efficiently, leading to localized stress concentrations and altered failure modes [96–98].

5.2. Effect of relative density

The influence of relative density on the mechanical properties of both the baseline (Lat1 N) and modified (Lat1 S) structures was systematically investigated. Fig. 29 plots the quasi-static and dynamic yield stress, plateau stress, and the dynamic increase factor (DIF) as functions of the measured as-printed relative density (ρ_{PR}). Quasi-static values serve as a baseline reference.

As anticipated from cellular mechanics theory, both the yield stress (Fig. 29(a)) and the plateau stress (Fig. 29(b)) exhibit a clear and strong positive correlation with relative density. Increasing the density from approximately 9% (ρ_R = 5%) to 21% (ρ_R = 15%) leads to a substantial rise in these strength metrics under both quasi-static and dynamic conditions (e.g., quasi-static plateau stress increases from $\sim$ 6 MPa to $\sim$ 40 MPa). This confirms that incorporating more material via denser architectures significantly enhances the load-bearing capacity and resistance to plastic deformation.

Examining the dynamic enhancement factor, DIF, as a function of relative density (Fig. 29(c)) reveals an interesting trend. At lower relative densities ($\rho_{PR} \approx 9\%$), the DIF values exhibit a wider spread, ranging from approximately 1.15 to 1.85. As the relative density increases, this variability diminishes, and the DIF values tend to converge towards a narrower range, roughly 1.15 to 1.45, particularly for the higher impact pressure (P = 0.25 MPa) tests. This suggests that while lower-density structures experience a potentially larger relative increase in strength under dynamic loading, their dynamic response might be more variable. Conversely, higher-density structures exhibit more consistent and predictable dynamic behavior relative to their quasi-static performance. The reduced variability in DIF at higher densities might reflect improved structural integrity and more uniform stress distribution, mitigating localized effects that could amplify dynamic response variations in less dense lattices.

Overall, this analysis underscores the fundamental role of relative density in governing the mechanical performance of these auxetic lattices. Increasing density directly enhances strength (yield and plateau stress) under both static and dynamic conditions. While the relative dynamic enhancement (DIF) might be more pronounced at lower densities, the absolute dynamic strength and the consistency of the dynamic response improve significantly with increasing density, leading to stronger and more predictable behavior in denser configurations under impact loading.

6. Conclusions and future perspectives

This study systematically investigated the quasi-static and dynamic compressive behavior of SLM-fabricated 316L stainless steel double-arrowhead auxetic lattice structures, focusing on the effects of relative density (5%, 10%, 15%) and a specific geometric modification: enlarging the 'stuffer' elements while reducing the 'tendon' elements (Lat1 S configuration) compared to a baseline design with equal elements (Lat1 N). Utilizing a combination of experimental testing (quasi-static compression, SHPB) and validated Finite Element Modeling (FEM) incorporating a Johnson–Cook constitutive model, we characterized deformation mechanisms, mechanical properties, energy absorption, and auxetic behavior. A key aspect enabling this work was the implementation of a precise density control algorithm during the design phase, ensuring high fidelity between target and as-printed relative densities.

The primary findings of this research are:

1. **Effect of Relative Density:** As expected, increasing the relative density significantly enhanced the mechanical performance for both Lat1 N and Lat1 S configurations. Yield stress, plateau stress, energy absorption per volume (W), and specific energy absorption (SEA) all demonstrated a strong positive correlation with relative density under both quasi-static and dynamic loading conditions.

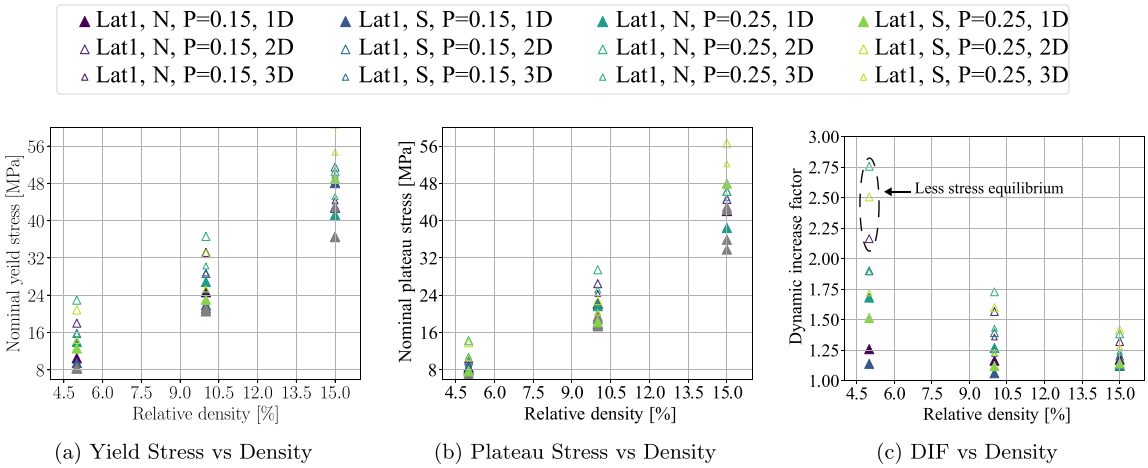

(a) Yield Stress vs Density (b) Plateau Stress vs Density (c) DIF vs Density

Fig. 29. Influence of measured relative density (ρ_{PR}) on mechanical properties: (a) quasi-static and dynamic yield stress, (b) quasi-static and dynamic plateau stress, and (c) Dynamic Increase Factor (DIF) based on plateau stress. Dynamic results shown for $P = 0.15$ and $P = 0.25$ MPa impacts using 3D analysis.

2. **Effect of Geometric Modification** (Lat1 S **vs.** Lat1 N): The modified Lat1 S configuration consistently demonstrated superior mechanical performance compared to the baseline Lat1 N, particularly at higher relative densities. *Strength:* At 15% relative density, Lat1 S exhibited significantly higher quasi-static plateau stress (42.0 MPa vs. 35.0 MPa for Lat1 N, a 21% increase) and dynamic plateau stress under $P = 0.25$ MPa impact (48.0 MPa vs. 38.5 MPa for Lat1 N, a 24% increase). Corresponding yield stresses also showed enhancement for Lat1 S at 15% density (quasi-static: 42.49 vs 36.5 MPa; dynamic: 48.98 vs 41.24 MPa). *Energy Absorption:* Lat1 S achieved superior energy absorption, particularly at higher densities. Quasi-statically, its W at densification was up to 20% higher than Lat1 N (10.67 vs 8.92 MJ/m^3 at 15% density). Dynamically, its SEA reached up to 32 J/g at 15% density, compared to 28 J/g for Lat1 N at maximum achieved strain. *Deformation Stability:* The Lat1 S design exhibited delayed densification strain at lower/intermediate densities and demonstrated enhanced structural stability with reduced lateral bulging and buckling tendencies, especially under dynamic loading, compared to Lat1 N.

3. **Strain Rate Sensitivity:** Both configurations exhibited significant strain rate sensitivity, with dynamic yield and plateau stresses markedly higher than quasi-static values. The Dynamic Increase Factor (DIF) ranged from approximately 1.15 to 1.85 over the tested strain rates (150–500 s^{-1}), increasing with strain rate. The dynamic enhancement was more consistent (less variable DIF) at higher relative densities.

4. **Auxetic Behavior:** Both designs displayed auxetic behavior (negative Poisson's ratio) during initial compression. The magnitude of the negative Poisson's ratio decreased with increasing relative density. Subtle differences were observed between Lat1 N and Lat1 S, with Lat1 N showing slightly stronger initial auxeticity at lower densities, while Lat1 S maintained better lateral stability overall, particularly at higher densities.

5. **Model Validation:** The FEM simulations, using a calibrated Johnson–Cook model and geometries adjusted for printed density, showed strong agreement with experimental stress–strain curves and deformation modes under both quasi-static and dynamic conditions (typically < 13% discrepancy in plateau stress), validating the numerical approach for predicting the behavior of these structures.

In conclusion, this study demonstrates that strategically modifying the internal geometry of double-arrowhead auxetic lattices — specifically by employing larger stuffers and smaller tendons (Lat1 S design) — significantly enhances compressive strength, energy absorption capacity, and deformation stability, particularly at higher relative densities and under dynamic loading conditions. The improved performance of Lat1 S is attributed to better load distribution facilitated by the enlarged stuffers. These findings highlight a promising pathway for optimizing auxetic metamaterials for demanding protective applications requiring high energy dissipation and structural integrity under impact. The validated FEM framework provides a reliable tool for further design exploration and optimization.

Future work should explore the performance of these optimized structures under more complex loading scenarios, such as multi-axial compression or combined compression–shear loading, which are often relevant in real-world impact events. Investigating alternative auxetic topologies and the potential of functionally graded density designs could offer further avenues for tailoring energy absorption characteristics. Additionally, exploring the influence of different SLM process parameters and post-processing treatments on the microstructure and resulting mechanical properties would provide a more comprehensive understanding for manufacturing robust and reliable auxetic components.

CRediT authorship contribution statement

Junsong Wang: Writing – original draft, Investigation, Software, Conceptualization, Data curation. **Cristoforo Demartino:** Investigation, Methodology, Conceptualization, Supervision, Funding acquisition. **Antonio P. Sberna:** Conceptualization, Methodology, Writing – review & editing. **Liming Jiang:** Methodology, Supervision, Writing – review & editing. **Asif Usmani:** Methodology, Supervision, Writing – review & editing.

Declaration of competing interest

The authors declare that they have no known competing financial interests or personal relationships that could have appeared to influence the work reported in this paper.

Acknowledgments

The research reported in this article was supported by the Hong Kong Polytechnic University, Department of Building Environment and Energy Engineering. This work was partially supported by the Zhejiang University/the University of Illinois at Urbana–Champaign Institute. The authors acknowledge Bangwei LIU (research assistant of ZJUI), Yating SUN (undergraduate student of ZJUI), and Haoran YE (undergraduate student of ZJUI) for helping in the DIC recording and analysis presented in this study.

Appendix A. DIC deformation analysis

See Figs. A.30–A.32.

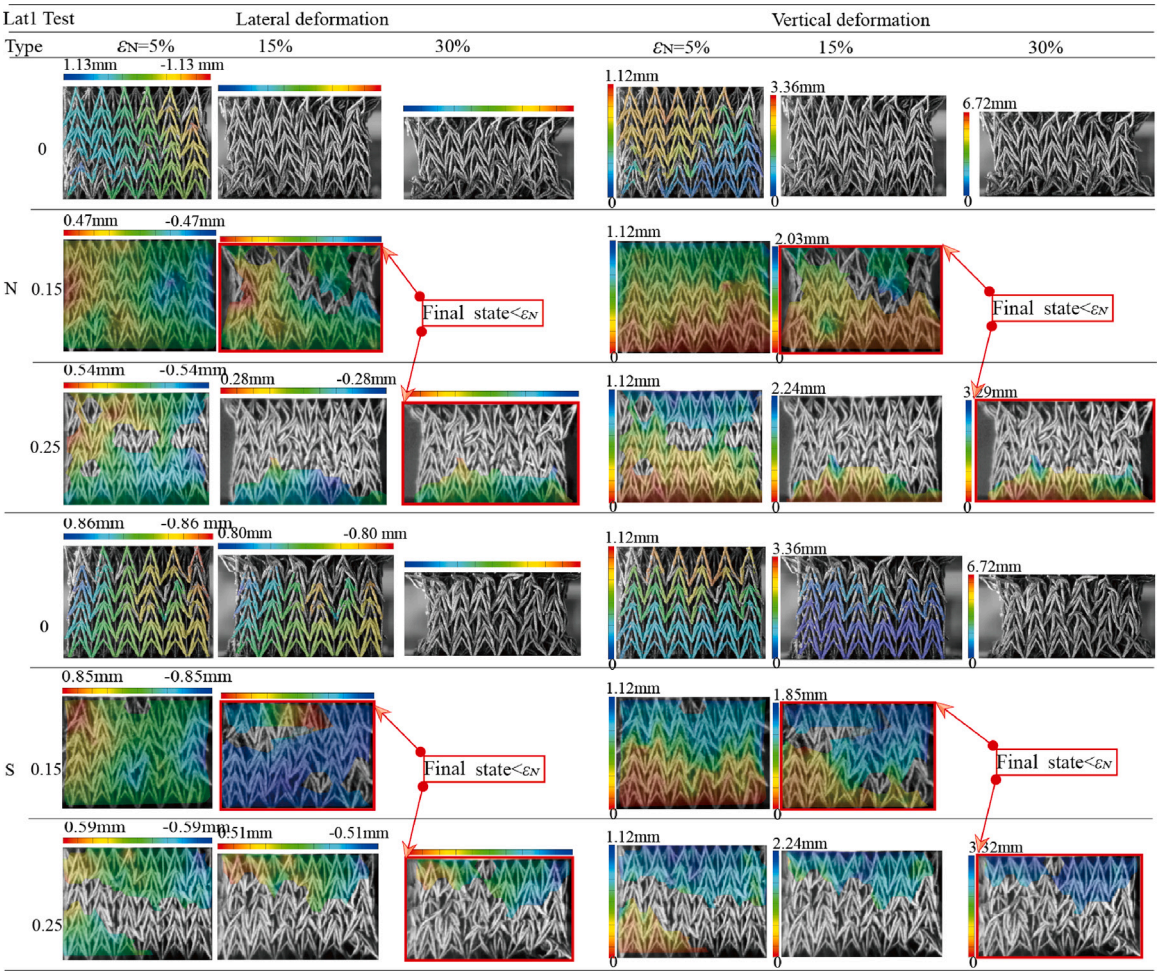

Fig. A.30. DIC deformation analysis along vertical and lateral direction, $\rho_R = 5\%$.

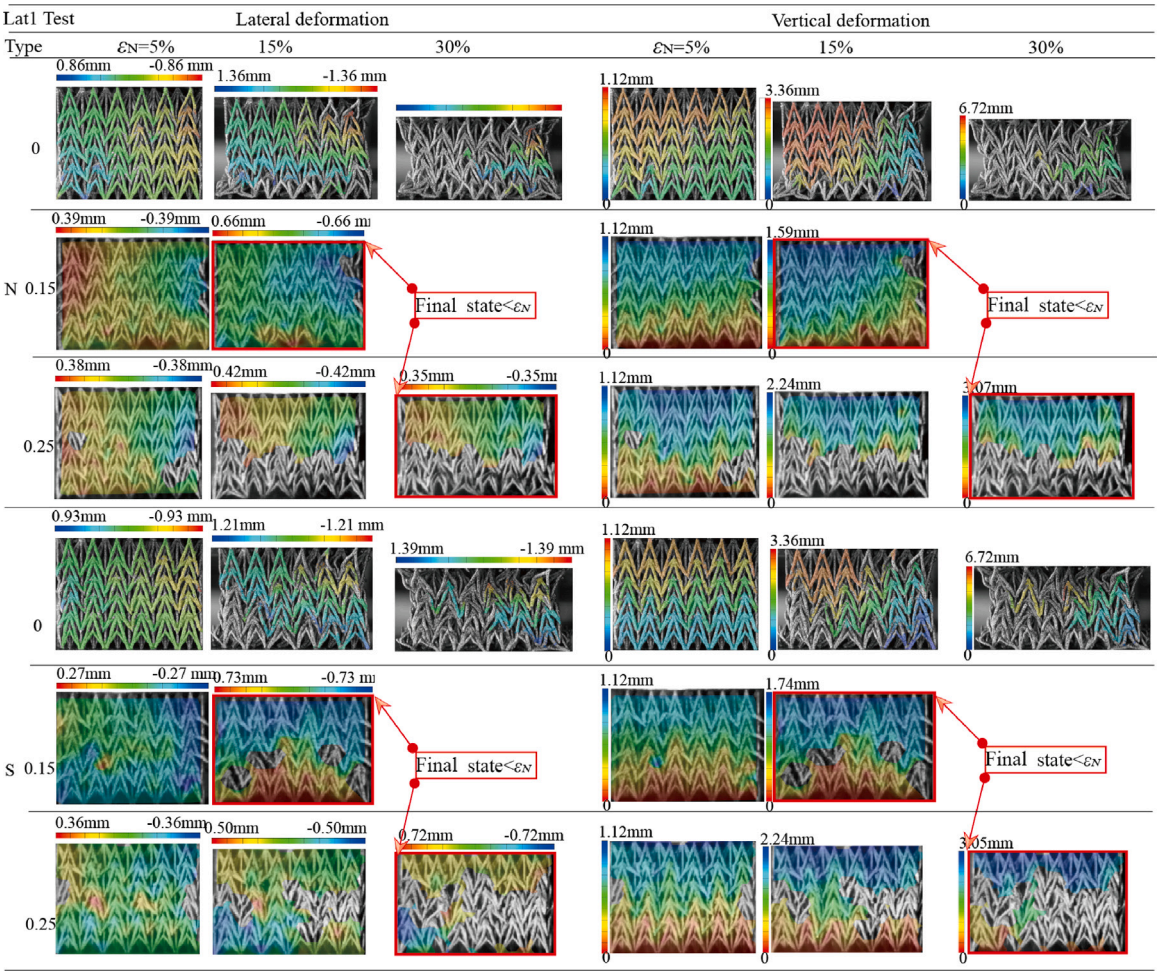

Fig. A.31. DIC deformation analysis along vertical and lateral direction, $\rho_R = 10\%$.

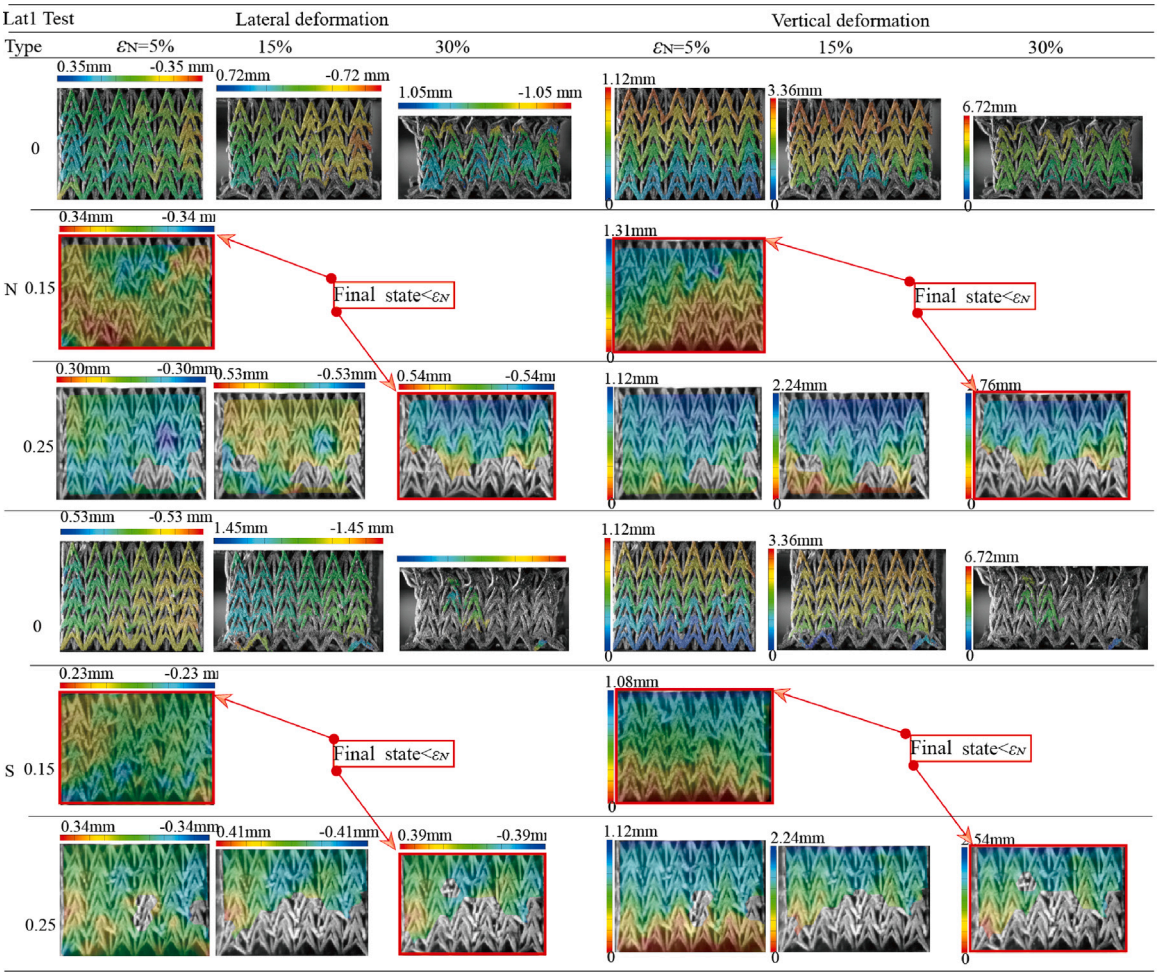

Fig. A.32. DIC deformation analysis along vertical and lateral direction, $\rho_R = 15\%$.

Appendix B. FEM stress and deformation distributions

See Tables B.7–B.9.

Table B.7
FEM stress (a) and deformation (b) distributions, $\rho_R = 5\%$. Note: Dashed lines: deformation contours; Gray box: original geometry.

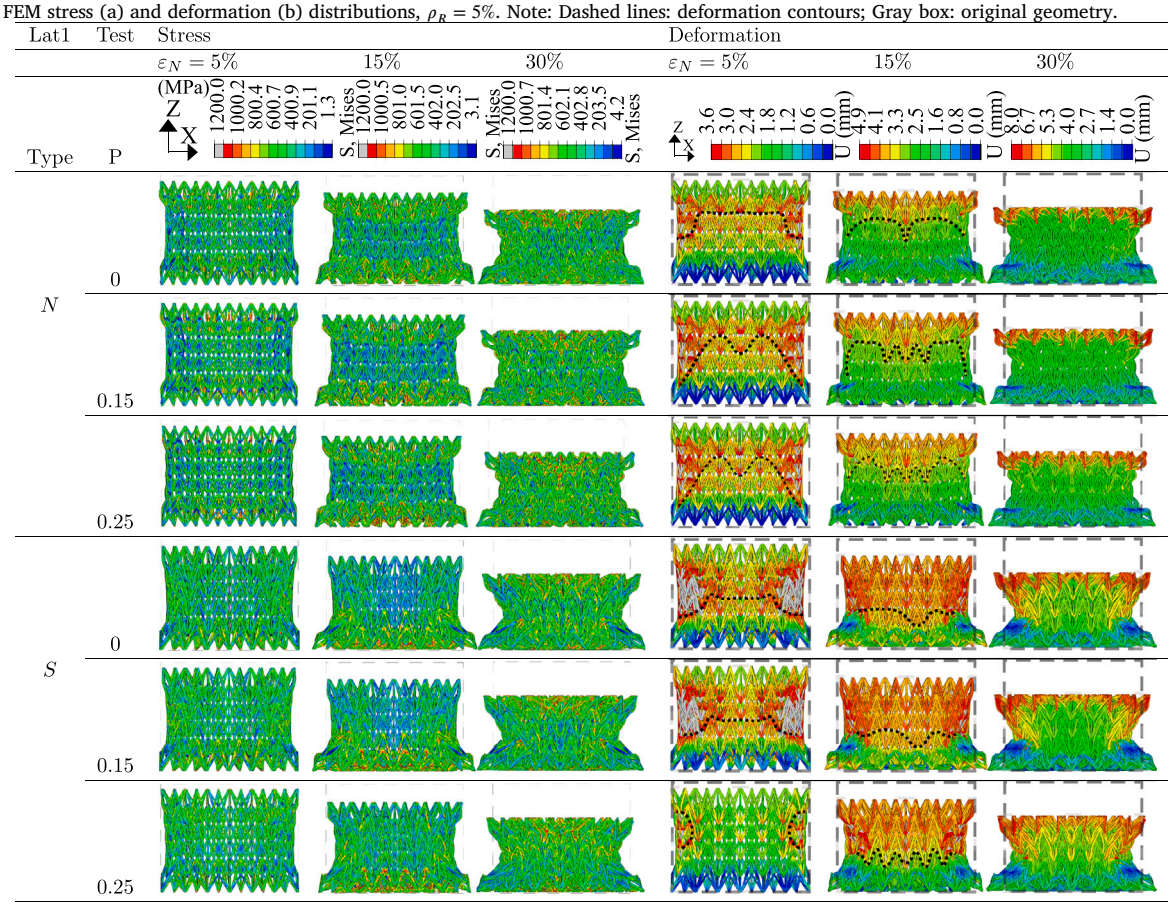

Table B.8
FEM stress (a) and deformation (b) distributions, $\rho_R = 10\%$. Note: Dashed lines: deformation contours; Gray box: original geometry.

Lat1	Test	Stress			Deformation		
		$\varepsilon_N = 5\%$	15%	30%	$\varepsilon_N = 5\%$	15%	30%
Type	P	(MPa) 1200.0 1000.2 800.4 600.7 400.9 201.1 1.3 S, Mises	1200.0 1000.5 801.0 601.5 402.0 202.5 3.1 S, Mises	1200.0 1000.7 801.4 602.1 402.8 203.5 4.2 S, Mises	Z X 3.6 3.0 2.4 1.8 1.2 0.6 0.0 U (mm)	4.9 4.1 3.3 2.5 1.6 0.8 0.0 U (mm)	8.0 6.7 5.3 4.0 2.7 1.4 0.0 U (mm)
N	0	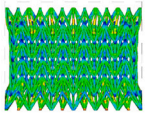	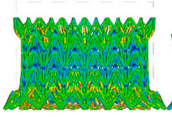	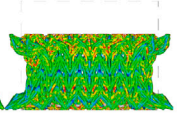	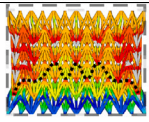	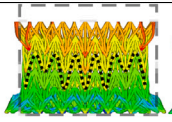	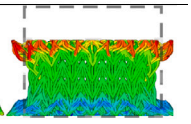
	0.15	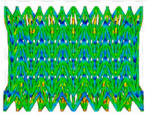	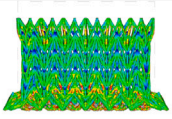	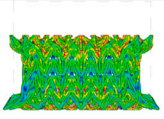	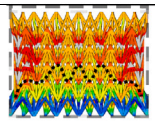	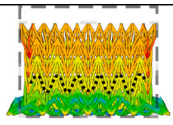	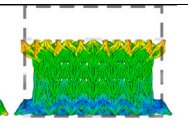
	0.25	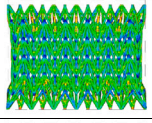	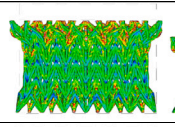	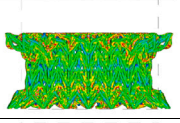	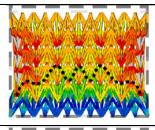	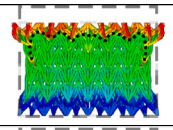	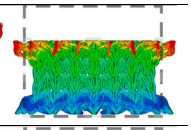
S	0	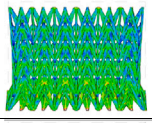	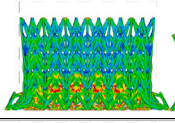	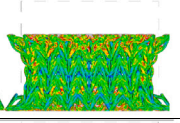	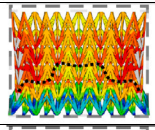	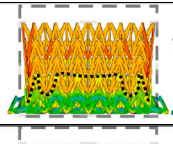	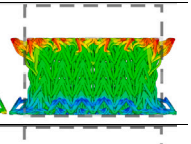
	0.15	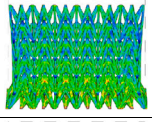	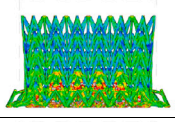	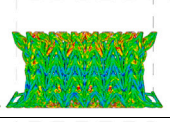	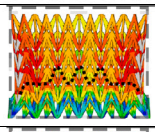	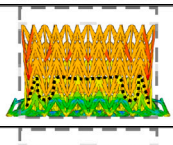	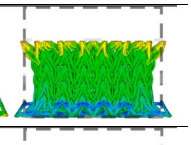
	0.25	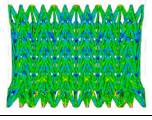	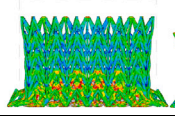	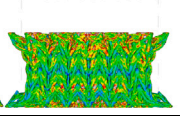	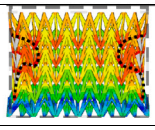	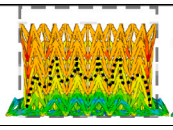	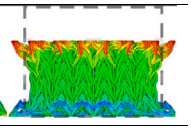

Table B.9
FEM stress (a) and deformation (b) distributions, $\rho_R = 15\%$. Note: Dashed lines: deformation contours; Gray box: original geometry.

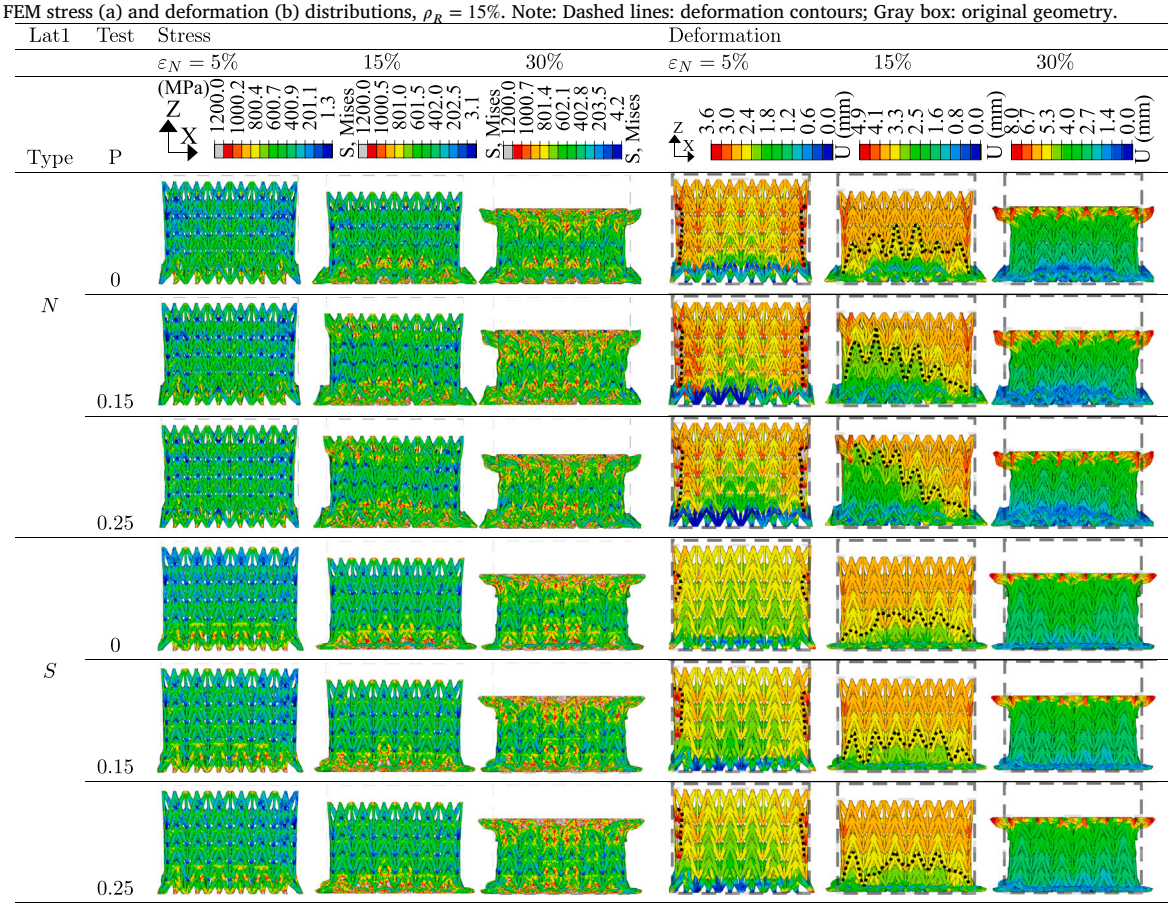

Data availability

Data will be made available on request.

References

[1] Maconachie T, Leary M, Lozanovski B, Zhang X, Qian M, Faruque O, et al. SLM lattice structures: Properties, performance, applications and challenges. Mater Des 2019;183:108137. http://dx.doi.org/10.1016/j.matdes.2019.108137.

[2] Evans KE, Nkansah MA, Hutchinson IJ, Rogers SC. Molecular network design. Nature 1991;353:124. http://dx.doi.org/10.1038/353124a0.

[3] Lakes RS, Elms K. Indentability of conventional and negative Poisson's ratio foams. J Compos Mater 1993;27:1193–202. http://dx.doi.org/10.1177/002199839302701203.

[4] Greaves GN, Greer AL, Lakes RS, Rouxel T. Poisson's ratio and modern materials. Nat Mater 2011;10:823–37. http://dx.doi.org/10.1038/nmat3134.

[5] Nian Y, Wan S, Avcar M, Wang X, Hong R, Yue R, et al. Nature-inspired 3D printing-based double-graded aerospace negative Poisson's ratio metastructure: Design, fabrication, investigation, optimization. Compos Struct 2024;348:118482.

[6] Bashtani M, Etemadi E, Hu H, Moradi M. Auxetic lattice structures consisting of an enhanced trigram frame unit cell with superior stiffness. Compos Struct 2024;338:118100.

[7] Zhang Y, Jiang W-Z, Jiang W, Zhang X-Y, Dong J, Xie Y-M, et al. Recent advances of auxetic metamaterials in smart materials and structural systems. Adv Funct Mater 2025;2421746.

[8] Zhang J, Lu G, You Z. Large deformation and energy absorption of additively manufactured auxetic materials and structures: A review. Compos Part B: Eng 2020;201:108340. http://dx.doi.org/10.1016/j.compositesb.2020.108340.

[9] Dubrovski PD, Novak N, Borovinsek M, Vesenjak M, Ren Z. In-plane deformation behavior and the open area of rotating squares in an auxetic compound fabric. Polymers 2022;14:571. http://dx.doi.org/10.3390/polym14030571.

[10] Xue Y, Han F. Compressive mechanical property of a new three-dimensional aluminum based double-V lattice structure. Mater Lett 2019;254:99–102. http://dx.doi.org/10.1016/j.matlet.2019.07.048.

[11] Carneiro VH, Puga H, Meireles J. Positive, zero and negative Poisson's ratio non-stochastic metallic cellular solids: Dependence between static and dynamic mechanical properties. Compos Struct 2019;226:111239. http://dx.doi.org/10.1016/j.compstruct.2019.111239.

[12] Kooistra GW, Deshpande VS, Wadley HNG. Compressive behavior of age hardenable tetrahedral lattice truss structures made from aluminium. Acta Mater 2004;52:4229–37. http://dx.doi.org/10.1016/j.actamat.2004.05.039.

[13] Queheillalt DT, Murty Y, Wadley HNG. Mechanical properties of an extruded pyramidal lattice truss sandwich structure. Scr Mater 2008;58:76–9. http://dx.doi.org/10.1016/j.scriptamat.2007.08.041.

[14] Fan H, Zeng T, Fang D, Yang W. Mechanics of advanced fiber reinforced lattice composites. Acta Mech Sin 2010;26:825–35. http://dx.doi.org/10.1007/s10409-010-0390-z.

[15] Fan H, Sun F, Yang L, Jin F, Zhao D. Interlocked hierarchical lattice materials reinforced by woven textile sandwich composites. Compos Sci Technol 2013;87:142–8. http://dx.doi.org/10.1016/j.compscitech.2013.07.028.

[16] Li W, Sun F, Wang P, Fan H, Fang D. A novel carbon fiber reinforced lattice truss sandwich cylinder: Fabrication and experiments. Compos Part A: Appl Sci Manuf 2016;81:313–22. http://dx.doi.org/10.1016/j.compositesa.2015.11.034.

[17] Wu Y, Fang J, Wu C, Li C, Sun G, Li Q. Additively manufactured materials and structures: A state-of-the-art review on their mechanical characteristics and energy absorption. Int J Mech Sci 2023;246:108102. http://dx.doi.org/10.1016/j.ijmecsci.2023.108102.

[18] Choi JB, Lakes RS. Non-linear properties of metallic cellular materials with a negative Poisson's ratio. J Mater Sci 1992;27:5375–81. http://dx.doi.org/10.1007/bf00553421.

[19] Kolpakov AG. Determination of the average characteristics of elastic frameworks. J Appl Math Mech 1985;49:739–45. http://dx.doi.org/10.1016/0021-8928(85)90011-5.

[20] Lakes R. Foam structures with a negative Poisson's ratio. Science 1987;235:1038–40. http://dx.doi.org/10.1126/science.235.4792.1038.

[21] Friis EA, Lakes RS, Park JB. Negative Poisson's ratio polymeric and metallic foams. J Mater Sci 1988;23:4406–14. http://dx.doi.org/10.1007/bf00551939.

[22] Chan N, Evans KE. The mechanical properties of conventional and auxetic foams. Part I: Compression and tension. J Cell Plast 1999;35:130–65. http://dx.doi.org/10.1177/0021955x9903500204.

[23] Barthelat F, Tang H, Zavattieri P, Li C, Espinosa H. On the mechanics of mother-of-pearl: A key feature in the material hierarchical structure. J Mech Phys Solids 2007;55:306–37. http://dx.doi.org/10.1016/j.jmps.2006.07.007.

[24] Grima JN, Attard D, Gatt R, Cassar RN. A novel process for the manufacture of auxetic foams and for their re-conversion to conventional form. Adv Eng Mater 2009;11:533–5. http://dx.doi.org/10.1002/adem.200800388.

[25] Bianchi M, Frontoni S, Scarpa F, Smith CW. Density change during the manufacturing process of PU-PE open cell auxetic foams. Phys Status Solidi (B) 2010;248:30–8. http://dx.doi.org/10.1002/pssb.201083966.

[26] Critchley R, Corni I, Wharton JA, Walsh FC, Wood RJK, Stokes KR. A review of the manufacture, mechanical properties and potential applications of auxetic foams. Phys Status Solidi (B) 2013;250:1963–82. http://dx.doi.org/10.1002/pssb.201248550.

[27] Zhang GH, Ghita O, Evans KE. The fabrication and mechanical properties of a novel 3-component auxetic structure for composites. Compos Sci Technol 2015;117:257–67. http://dx.doi.org/10.1016/j.compscitech.2015.06.012.

[28] Reda H, Rahali Y, Ganghoffer JF, Lakiss H. Wave propagation in 3D viscoelastic auxetic and textile materials by homogenized continuum micropolar models. Compos Struct 2016;141:328–45. http://dx.doi.org/10.1016/j.compstruct.2016.01.071.

[29] Lakes RS. Design considerations for materials with negative Poisson's ratios. J Mech Des 1993;115:696–700. http://dx.doi.org/10.1115/1.2919256.

[30] Howell B, Prendergast P, Hansen L. Examination of acoustic behavior of negative poisson's ratio materials. Appl Acoust 1994;43:141–8. http://dx.doi.org/10.1016/0003-682x(94)90057-4.

[31] Scarpa F, Tomlin PJ. On the transverse shear modulus of negative Poisson's ratio honeycomb structures. Fatigue Fract Eng Mater Struct 2000;23:717–20. http://dx.doi.org/10.1046/j.1460-2695.2000.00278.x.

[32] Bianchi M, Scarpa FL, Smith CW. Stiffness and energy dissipation in polyurethane auxetic foams. J Mater Sci 2008;43:5851–60. http://dx.doi.org/10.1007/s10853-008-2841-5.

[33] Donoghue JP, Alderson KL, Evans KE. The fracture toughness of composite laminates with a negative Poisson's ratio. Phys Status Solidi (B) 2009;246:2011–7. http://dx.doi.org/10.1002/pssb.200982031.

[34] Oh J-H, Kim J-S, Nguyen VH, Oh I-K. Auxetic graphene oxide-porous foam for acoustic wave and shock energy dissipation. Compos Part B: Eng 2020;186:107817. http://dx.doi.org/10.1016/j.compositesb.2020.107817.

[35] Taylor M, Francesconi L, Gerendas M, Shanian A, Carson C, Bertoldi K. Low porosity metallic periodic structures with negative Poisson's ratio. Adv Mater 2013;26:2365–70. http://dx.doi.org/10.1002/adma.201304464.

[36] Xiong J, Gu D, Chen H, Dai D, Shi Q. Structural optimization of re-entrant negative Poisson's ratio structure fabricated by selective laser melting. Mater Des 2017;120:307–16. http://dx.doi.org/10.1016/j.matdes.2017.02.022.

[37] Yang H, Wang B, Ma L. Mechanical properties of 3D double-U auxetic structures. Int J Solids Struct 2019;180–181:13–29. http://dx.doi.org/10.1016/j.ijsolstr.2019.07.007.

[38] Hu LL, Wu ZJ, Fu MH. Mechanical behavior of anti-trichiral honeycombs under lateral crushing. Int J Mech Sci 2018;140:537–46. http://dx.doi.org/10.1016/j.ijmecsci.2018.03.039.

[39] Xue Y, Wang X, Wang W, Zhong X, Han F. Compressive property of Al-based auxetic lattice structures fabricated by 3-D printing combined with investment casting. Mater Sci Eng: A 2018;722:255–62. http://dx.doi.org/10.1016/j.msea.2018.02.105.

[40] Hu LL, Luo ZR, Zhang ZY, Lian MK, Huang LS. Mechanical property of re-entrant anti-trichiral honeycombs under large deformation. Compos Part B: Eng 2019;163:107–20. http://dx.doi.org/10.1016/j.compositesb.2018.11.010.

[41] Gao G, Li H, Lu H, Ren W, Zhong Y, Lei Z. Investigation into the quasi-static/dynamic combined shear-compression behaviors of three honeycomb like structures. Compos Struct 2025;352:118639.

[42] Choi JB, Lakes RS. Design of a fastener based on negative Poisson's ratio foam. Cell Polym 1991;10:205–12. http://dx.doi.org/10.1177/026248939101000302.

[43] Scarpa F, Giacomin J, Zhang Y, Pastorino P. Mechanical performance of auxetic polyurethane foam for antivibration glove applications. Cell Polym 2005;24:253–68. http://dx.doi.org/10.1177/026248930502400501.

[44] Iesan D. Pressure vessel problem for chiral elastic tubes. Internat J Engrg Sci 2011;49:411–9. http://dx.doi.org/10.1016/j.ijengsci.2011.01.003.

[45] Ali MN, Busfield JJC, Rehman IU. Auxetic oesophageal stents: Structure and mechanical properties. J Mater Sci, Mater Med 2013;25:527–53. http://dx.doi.org/10.1007/s10856-013-5067-2.

[46] Yang C, Vora HD, Chang Y. Behavior of auxetic structures under compression and impact forces. Smart Mater Struct 2018;27:025012. http://dx.doi.org/10.1088/1361-665x/aaa3cf.

[47] Lu X, Lin X, Chiumenti M, Cervera M, Li J, Ma L, et al. Finite element analysis and experimental validation of the thermomechanical behavior in laser solid forming of Ti–6Al–4V. Addit Manuf 2018;21:30–40. http://dx.doi.org/10.1016/j.addma.2018.02.003.

[48] Mugwagwa L, Dimitrov D, Matope S, Yadroitsev I. Influence of process parameters on residual stress related distortions in selective laser melting. Procedia Manuf 2018;21:92–9. http://dx.doi.org/10.1016/j.promfg.2018.02.099, 15th Global Conference on Sustainable Manufacturing.

[49] Jafari D, Wits WW, Vaneker THJ, Demir AG, Previtali B, Geurts BJ, et al. Pulsed mode selective laser melting of porous structures: Structural and thermophysical characterization. Addit Manuf 2020;35:101263. http://dx.doi.org/10.1016/j.addma.2020.101263.

[50] Zhai W, Zhou W, Nai SML. Grain refinement and strengthening of 316L stainless steel through addition of TiC nanoparticles and selective laser melting. Mater Sci Eng: A 2022;832:142460. http://dx.doi.org/10.1016/j.msea.2021.142460.

[51] Tan C, Zhou K, Kuang M, Ma W, Kuang T. Microstructural characterization and properties of selective laser melted maraging steel with different build directions. Sci Technol Adv Mater 2018;19:746–58.

[52] Han SJ, Bang GB, Kim WR, Kim GH, Kang H-S, Han HS, et al. Effect on microstructural and mechanical properties of selective laser melted pure Ti parts using stress relief heat-treatment process. J Mater Res Technol 2023;27:200–8. http://dx.doi.org/10.1016/j.jmrt.2023.09.288.

[53] Bartolomeu F, Costa MM, Alves N, Miranda G, Silva FS. Selective laser melting of Ti6Al4V sub-millimetric cellular structures: Prediction of dimensional deviations and mechanical performance. J Mech Behav Biomed Mater 2021;113:104123. http://dx.doi.org/10.1016/j.jmbbm.2020.104123.

[54] Huang L, Cao Y, Li G, Wang Y. Microstructure characteristics and mechanical behaviour of a selective laser melted Inconel 718 alloy. J Mater Res Technol 2020;9:2440–54. http://dx.doi.org/10.1016/j.jmrt.2019.12.075.

[55] Guo M-F, Yang H, Zhou Y-M, Ma L. Mechanical properties of 3D hybrid double arrow-head structure with tunable Poisson's ratio. Aerosp Sci Technol 2021;119:107177. http://dx.doi.org/10.1016/j.ast.2021.107177.

[56] ASTM International. F3184-16: Standard specification for additive manufacturing stainless steel alloy (UNS S31603) with powder bed fusion. 2016, ASTM International, West Conshohocken, PA, USA.

[57] ASTM International. A484/A484M-23: Standard specification for general requirements for stainless steel bars, billets, and forgings. 2016, ASTM International, West Conshohocken, PA, USA.

[58] Wu XJ, Gorham DA. Stress equilibrium in the split Hopkinson pressure bar test. J Phys IV 1997;7:C3–91.

[59] Xiong B, Wang J, Benidir A, Demartino C, Xiao Y. Design and calibration of a large-scale 155 mm split-Hopkinson pressure bar. J Mater Civ Eng 2024;36:04023591.

[60] Gray III GT. Classic split Hopkinson pressure bar testing. ASM Handb 2000;8:462–76.

[61] Gama BA, Lopatnikov SL, Gillespie Jr JW. Hopkinson bar experimental technique: A critical review. Appl Mech Rev 2004;57:223–50.

[62] Brizard D, Ronel S, Jacquelin E. Estimating measurement uncertainty on stress–strain curves from SHPB. Exp Mech 2017;57:735–42.

[63] Jiang TZ, Xue P, Butt HSU. Pulse shaper design for dynamic testing of viscoelastic materials using polymeric SHPB. Int J Impact Eng 2015;79:45–52.

[64] Deshpande VM, Madan S, Chakraborty T. Experimental and numerical study on designing pulse shapers for testing rocks in large-diameter SHPB. J Mater Civ Eng 2023;35:04023012.

[65] Chen X, Ge L, Zhou J, Wu S. Experimental study on split Hopkinson pressure bar pulse-shaping techniques for concrete. J Mater Civ Eng 2016;28:04015196.

[66] Song Z, Wang Z, Kim H, Ma H. Pulse shaper and dynamic compressive property investigation on ice using a large-sized modified split Hopkinson pressure bar. Lat Am J Solids Struct 2016;13:391–406.

[67] Hassan M, Wille K. Experimental impact analysis on ultra-high performance concrete for achieving stress equilibrium and constant strain rate in split Hopkinson pressure bar using pulse shaping technique. Constr Build Mater 2017;144:747–57.

[68] Wang J, Li W, Xu L, Du Z, Gao G. Experimental study on pulse shaping techniques of large diameter SHPB apparatus for concrete. Lat Am J Solids Struct 2021;18.

[69] Khanna P, Sood S, Mishra P, Bharadwaj V, Aggarwal A, Singh SJ. Analysis of compression and energy absorption behaviour of SLM printed AlSi10Mg triply periodic minimal surface lattice structures. Structures 2024;64:106580. http://dx.doi.org/10.1016/j.istruc.2024.106580.

[70] Gibson LJ, Ashby MF. Cellular Solids : Structure and Properties. 1997.

[71] Bai L, Zhang J, Xiong Y, Chen X, Sun Y, Gong C, et al. Influence of unit cell pose on the mechanical properties of Ti6Al4V lattice structures manufactured by selective laser melting. Addit Manuf 2020;34:101222. http://dx.doi.org/10.1016/j.addma.2020.101222.

[72] Duan Y, Du B, Shi X, Hou B, Li Y. Quasi-static and dynamic compressive properties and deformation mechanisms of 3D printed polymeric cellular structures with Kelvin cells. Int J Impact Eng 2019;132:103303. http://dx.doi.org/10.1016/j.ijimpeng.2019.05.017.
[73] Lei H, Li C, Meng J, Zhou H, Liu Y, Zhang X, et al. Evaluation of compressive properties of SLM-fabricated multi-layer lattice structures by experimental test and μ-CT-based finite element analysis. Mater Des 2019;169:107685. http://dx.doi.org/10.1016/j.matdes.2019.107685.
[74] Yang C, Di Ouyang, Zhang L, Zhang Y, Tong X, Ke H, et al. The enhancement of damage tolerance of 3D-printed high strength architected metallic glasses by unit cell shape design. Addit Manuf 2024;85:104125. http://dx.doi.org/10.1016/j.addma.2024.104125, URL: https://www.sciencedirect.com/science/article/pii/S2214860424001714.
[75] Al-Ketan O, Rowshan R, Abu Al-Rub RK. Topology-mechanical property relationship of 3D printed strut, skeletal, and sheet based periodic metallic cellular materials. Addit Manuf 2018;19:167–83. http://dx.doi.org/10.1016/j.addma.2017.12.006.
[76] Funch CV, Proust G. Laser-based additive manufacturing of refractory metals and their alloys: A review. Addit Manuf 2024;94:104464.
[77] Zhao R, Guo S, Zhang F, Zhang W, Yang D, Yue X, et al. Enhanced energy absorption and low anisotropy of additively manufactured porous Ti–6Al–4V alloy with disordered trapezo-rhombic dodecahedron structures. Addit Manuf 2024;95:104557. http://dx.doi.org/10.1016/j.addma.2024.104557.
[78] Hu D, Wang J, Liao Z, Fu MW. Localized strengthening of triply periodic minimal surface lattice structures via tuning the internal material distribution at the grain level. Addit Manuf 2025;99:104663. http://dx.doi.org/10.1016/j.addma.2025.104663.
[79] Johnson GR, Cook WH. Fracture characteristics of three metals subjected to various strains, strain rates, temperatures and pressures. Eng Fract Mech 1985;21:31–48. http://dx.doi.org/10.1016/0013-7944(85)90052-9.
[80] Li P. Constitutive and failure behaviour in selective laser melted stainless steel for microlattice structures. Mater Sci Eng: A 2015;622:114–20. http://dx.doi.org/10.1016/j.msea.2014.11.028.
[81] Platek P, Sienkiewicz J, Janiszewski J, Jiang F. Investigations on mechanical properties of lattice structures with different values of relative density made from 316L by selective laser melting (SLM). Materials 2020;13. http://dx.doi.org/10.3390/ma13092204.
[82] Sandmann P, Keller S, Kashaev N, Ghouse S, Hooper PA, Klusemann B, et al. Influence of laser shock peening on the residual stresses in additively manufactured 316L by laser powder bed fusion: A combined experimental-numerical study. Addit Manuf 2022;60:103204. http://dx.doi.org/10.1016/j.addma.2022.103204.
[83] Xue H, Wang T, yu Cui X, fan Wang Y, yan Huang G. On the ballistic perforation performance of additively manufactured 316L stainless steel cylindrical projectiles. Int J Impact Eng 2023;178:104625. http://dx.doi.org/10.1016/j.ijimpeng.2023.104625.
[84] Alkhatib SE, Xu S, Lu G, Karrech A, Sercombe TB. Rate-dependent behaviour of additively manufactured topology optimised lattice structures. Thin-Walled Struct 2024;198:111710. http://dx.doi.org/10.1016/j.tws.2024.111710.
[85] Wang Z, Li P. Characterisation and constitutive model of tensile properties of selective laser melted Ti–6Al–4V struts for microlattice structures. Mater Sci Eng: A 2018;725:350–8. http://dx.doi.org/10.1016/j.msea.2018.04.006.
[86] Iqbal MA, Senthil K, Bhargava P, Gupta NK. The characterization and ballistic evaluation of mild steel. Int J Impact Eng 2015;78:98–113. http://dx.doi.org/10.1016/j.ijimpeng.2014.12.006.
[87] Cao X, Xiao D, Li Y, Wen W, Zhao T, Chen Z, et al. Dynamic compressive behavior of a modified additively manufactured rhombic dodecahedron 316L stainless steel lattice structure. Thin-Walled Struct 2020;148:106586. http://dx.doi.org/10.1016/j.tws.2019.106586.
[88] Cervinek O, Pettermann H, Todt M, Koutny D, Vaverka O. Non-linear dynamic finite element analysis of micro-strut lattice structures made by laser powder bed fusion. J Mater Res Technol 2022;18:3684–99. http://dx.doi.org/10.1016/j.jmrt.2022.04.051.
[89] Jin N, Wang F, Wang Y, Zhang B, Cheng H, Zhang H. Effect of structural parameters on mechanical properties of pyramidal kagome lattice material under impact loading. Int J Impact Eng 2019;132:103313. http://dx.doi.org/10.1016/j.ijimpeng.2019.06.002.
[90] Li X, Xiao L, Song W. Compressive behavior of selective laser melting printed gyroid structures under dynamic loading. Addit Manuf 2021;46:102054. http://dx.doi.org/10.1016/j.addma.2021.102054.
[91] Qiao J, Chen CQ. Analyses on the in-plane impact resistance of auxetic double arrowhead honeycombs. J Appl Mech 2015;82:051007.
[92] Gao Q, Liao W-H, Wang L. On the low-velocity impact responses of auxetic double arrowed honeycomb. Aerosp Sci Technol 2020;98:105698. http://dx.doi.org/10.1016/j.ast.2020.105698.
[93] Li Q, Zhi X, Fan F. Dynamic crushing of uniform and functionally graded origami-inspired cellular structure fabricated by SLM. Eng Struct 2022;262:114327. http://dx.doi.org/10.1016/j.engstruct.2022.114327.
[94] McKown S, Shen Y, Brookes WK, Sutcliffe CJ, Cantwell WJ, Langdon GS, et al. The quasi-static and blast loading response of lattice structures. Int J Impact Eng 2008;35:795–810. http://dx.doi.org/10.1016/j.ijimpeng.2007.10.005.
[95] Tancogne-Dejean T, Spierings AB, Mohr D. Additively-manufactured metallic micro-lattice materials for high specific energy absorption under static and dynamic loading. Acta Mater 2016;116:14–28. http://dx.doi.org/10.1016/j.actamat.2016.05.054.
[96] Tang X, Prakash V, Lewandowski JJ, Kooistra GW, Wadley HNG. Inertial stabilization of buckling at high rates of loading and low test temperatures: Implications for dynamic crush resistance of aluminum-alloy-based sandwich plates with lattice core. Acta Mater 2007;55:2829–40. http://dx.doi.org/10.1016/j.actamat.2006.12.037.
[97] Hou B, Zhao H, Pattofatto S, Liu JG, Li YL. Inertia effects on the progressive crushing of aluminium honeycombs under impact loading. Int J Solids Struct 2012;49:2754–62. http://dx.doi.org/10.1016/j.ijsolstr.2012.05.005.
[98] Liu J, Pattofatto S, Fang D, Lu F, Zhao H. Impact strength enhancement of aluminum tetrahedral lattice truss core structures. Int J Impact Eng 2015;79:3–13. http://dx.doi.org/10.1016/j.ijimpeng.2014.06.013.